S. Ubal
Instituto de Desarrollo Tecnológico
para la Industria Química,
UNL-CONICET,
Güemes 3450,
3000 Santa Fe (Capital), Argentina
e-mail: subal@santafe-conicet.gov.ar

B. Xu
e-mail: bojunxu.uk@gmail.com

B. Derby
e-mail: brian.derby@manchester.ac.uk

Materials Science Centre,
The University of Manchester,
Grosvenor Street,
Manchester M1 7HS, UK

P. Grassia[1]
CEAS,
The University of Manchester,
Oxford Road,
Manchester M13 9PL,UK
e-mail: paul.grassia@manchester.ac.uk

Continuous Deposition of a Liquid Thread onto a Moving Substrate. Numerical Analysis and Comparison With Experiments

The printing of a thin line of liquid onto a moving flat solid substrate was studied numerically. For a fixed value of the Capillary number, the window of steady state deposition was explored in terms of the substrate-nozzle gap and flow rate parameter space for two nozzle configurations: a nozzle pointing vertically at the plate and a nozzle slightly tilted towards the substrate motion direction. A lower limit for the flow rate was found, below which no steady state solutions could be obtained. This minimum flow rate increases as the nozzle stand-off and the nozzle tilting do. Solutions near this lower flow rate boundary were stable under a flow rate perturbation. The process was also studied experimentally and the measurements were compared with the corresponding numerical simulations, giving a fairly good agreement, except in the advancing front deposition region. [DOI: 10.1115/1.4005668]

1 Introduction

Depositing a thread of fluid on a solid substrate is a process having different applications ranging from food processing to printed electronics. Typically the fluid is continuously extruded from a narrow nozzle closely situated over a flat solid surface. They have a relative motion, resulting in the nozzle displacing at a certain distance above the substrate, tracing either a straight or a curved trajectory that results in a deposited thread of fluid following a similar global path.

This work is mainly motivated by printed electronics applications, where the fluid employed is commonly a polymeric melt with a high content of metal-containing particles. Once the fluid is deposited following a given specified pattern, a curing procedure is necessary to convert the liquid suspension into a conducting track. This form of printing electronic circuits is known as *Direct-Write* (or also Pen-Writing) [1–4]. Actually, Direct-Write is a general term employed to encompass a wide range of technologies with a common feature: they involve the delivery of (in most cases) material and/or energy from a small sized nozzle, tip or probe, onto a given substrate. In the context of printed electronics, the main advantages of Direct-Write compared to conventional mass production technologies (such as gravure, offset and flexographic printing) is the capacity for rapid prototyping and reduced development times, and the ability to print onto conformal/curved surfaces.

Since in most cases the desired result of the deposition process is a continuous (and possibly curved) line of fluid, it is important to identify the conditions under which the continuity of the liquid thread could be interrupted. We could identify two kinds of breakup processes: those taking place once the line of liquid is already deposited, and those occurring during the deposition process itself, typically near the nozzle extrusion region. It is worth noting that the timescale of these instability processes, scaling with fluid viscosity, is at most on the order of tens of seconds, much shorter than any drying/solidification timescale. At room temperature conditions, drying/solidification usually takes hours (and even days) for typical (non-volatile) ink formulations used in Direct-Write.

The former kind of rupture processes have been studied in Refs. [5–8]. The linear stability analyses of Refs. [5,6] predict that the liquid thread is unstable for any value of the (dynamic) contact angle when this is fixed or varying smoothly with the contact line speed, and for any contact angle larger than $\pi/2$ when the contact line is fixed. Reference [7] studies both kinds of boundary conditions experimentally. On the other hand, the experimental work in Ref. [8] reveals an instability and pinch-off process that progress from the ends to the center of a finite length line of liquid. In the context of drop-on-demand (rather than continuous) printing, Ref. [9] studies experimentally and theoretically the stability of the printed tracks when the liquid has a zero receding contact angle (i.e. the contact line can advance but not recede), considering that eventual instabilities could be initiated/influenced by the printing conditions.

On the contrary, the breakup of the liquid thread during continuous deposition seems to have received little attention; in fact, to our knowledge there are no published systematic studies of this phenomenon. In connection with the deposition process—but not addressing specifically the breakup phenomenon—Refs. [10] and [11] investigated experimentally and theoretically the bifurcation phenomena arising when the fluid is extruded at a constant flow rate from sufficiently high distances above the substrate: as the speed of the solid surface reduces, the shape of the deposited liquid thread changes from a straight line to different meandering states, including "simple" meanders, figure-of-8 shapes and loops. On the other hand, Ref. [12] has reported experimental measurements where, for a given substrate speed, there is a minimum flow rate, below which the liquid thread breaks-up near the nozzle exit; this minimum flow rate is known to increase as the extrusion nozzle is situated at a higher distance above the substrate.

[1]Corresponding author.

Contributed by the Fluids Engineering Division of ASME for publication in the JOURNAL OF FLUIDS ENGINEERING. Manuscript received August 24, 2011; final manuscript received November 15, 2011; published online March 6, 2012. Assoc. Editor: John Abraham.

Processes like curtain and slot coating, presenting some common features with the problem of interest in this paper, usually display instabilities leading to defects or the breakup of the coating film [13].

For large substrate speeds in particular, there are two well-known problems: air-entrainment in the front meniscus and a ribbing phenomenon (eventually leading to breakup into strips) in the trailing film [14].

The deposition problem has also been studied numerically by Ref. [15] (referred to hereafter as BAER), and Refs. [16] and [17], although the last two papers only show simulations for specific values of the parameters and the results, discussed only briefly, focus on the effect of the evaporation of one of the components of the fluid being deposited, rather on the fluid mechanics problem. On the other hand, the work by BAER [15] analyzes the influence of the flow rate, the Capillary number and the contact angle on the steady state fluid profile near the deposition region. The authors also carry out an experimental measurement of the process and compare it with the corresponding numerical prediction, achieving some qualitative agreement.

This work is also a numerical study of the liquid thread deposition with a focus on printed electronics applications. However, the emphasis in this paper is the systematic exploration of the steady state solution space, in terms of the flow rate and the nozzle-substrate gap distance (our focus is on distances of the order of the nozzle radius), for fixed values of the remaining parameters, and two different nozzle configurations: one with the nozzle pointing vertically to the substrate and the other with a small tilting angle. In either case, our model considers the finite width of the nozzle wall. The procedure employed allowed us to identify the limits of the steady state region. Besides, we carried out transient simulations to test the stability of the steady state results and to explore the behavior of the system outside the steady state operating window. We also obtained several experimental measurements of the process, which compare fairly well with the corresponding numerical computations. Our model assumes the fluid being a Newtonian liquid, and we employ Navier's slip condition to relieve the contact line singularity. As in BAER [15], we solve the governing equations using a numerical technique based on the Finite Element Method, combined with an Arbitrary Lagrangian-Eulerian methodology to follow the shape of the free surface, and therefore of the flow domain.

The structure of the paper is as follows. The next section contains the governing equations of the fluid dynamic model. Section 3 explains the numerical technique employed to solve the governing equations. The methodology employed to obtain the experimental results is detailed in Sec. 4. Section 5 shows the numerical results, both in steady and unsteady state, and Sec. 6 describes the comparison with the experimental measurements. Finally, in Sec. 7, our findings are summarized, and some possible future extensions are proposed.

2 The Physical Model

Let us consider a flat horizontal solid substrate whose surface is the plane $z=0$, in the rectangular coordinate system adopted for reference, as sketched in Fig. 1(*a*). Over the plane $z=0$ there is an inviscid gas phase at rest, whose constant pressure is adopted as the system pressure reference and is set equal to zero. The substrate moves at a constant and uniform velocity $V\mathbf{i}$ along the x-axis. Above the substrate, there is a motionless (with respect to the frame of reference) tube with a circular cross section, whose internal radius and wall thickness are both equal to R. The axis of the tube lies in the plane $y=0$ and possesses a tilting angle α with the z-axis, measured counterclockwise as shown in Fig. 1(*a*). The lower end of the tube—the tip of the nozzle—is a circular section whose center is situated at $(x, y, z)=(0, 0, R\mathcal{H})$. Fluid is pumped downwards through the tube, the flow rate being equal to $\pi R^2 V\mathcal{U}$. The fluid arising from the nozzle tip deposits on the moving substrate, forming a fluid filament whose free surface has a surface tension σ. Notice (see Fig. 1(*a*)) that our model considers that the

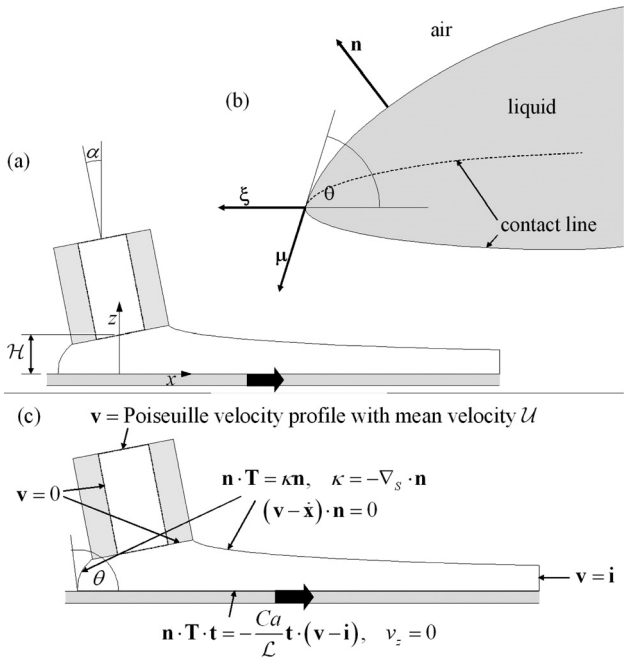

Fig. 1 Sketch of the physical model. (*a*) Definition of the coordinate system and geometrical parameters. (*b*) Definition of normal vectors on the contact line, one tangent to the substrate (ξ) and the other tangent to the free surface (μ). (*c*) Summary of boundary conditions employed in the model. Mathematical expressions are in dimensionless form.

fluid wets entirely the nozzle tip, but not its lateral wall, i.e., the contact line is pinned on the external edge of the nozzle tip.

Some (if not most) of the practical applications that motivated this work—particularly the direct-writing of electronic circuit tracks—employ complex fluids/inks that usually display complicated rheological behaviors, most visibly shear thinning (see Fig. 21 in Appendix A). However, for simplicity, we are assuming for the most part of this work that the fluid is a Newtonian liquid with viscosity (μ), density (ρ) and surface tension (σ), all constant. This hypothesis is strongly supported by the results shown in Appendix C, where we observe that the shear-thinning behavior of the fluid, for a realistic set of parameters, has a very small influence on the process. The typical operating conditions determine a shear rate regime on the order of 10 s^{-1}, a value above which the viscosity tends to have small changes with shear rate, as can be seen in Fig. 21. Besides, although thermal effects could be noticeable during the timescale of the deposition or instability processes, these usually take place at room conditions, so that the actual temperature variations are small enough (a few degrees) as to produce insignificant changes in material properties.

The conservation of momentum and mass in the liquid phase can be described by the Navier-Stokes and continuity equations, given in dimensionless form by

$$La\, Ca^2 \left(\frac{\partial \mathbf{v}}{\partial t} + \mathbf{v}\cdot\nabla\mathbf{v}\right) = -\nabla p + Ca\nabla^2\mathbf{v} - Bo\,\mathbf{k} \tag{1}$$

$$\nabla\cdot\mathbf{v} = 0 \tag{2}$$

where spatial variables are scaled by R, velocities by V, time by R/V and pressure by σ/R. The dimensionless parameters appearing in Eqs. (1)–(2) are the Capillary number ($Ca \equiv \mu V/\sigma$), the Laplace number ($La \equiv \rho\sigma R/\mu^2$) and the Bond number ($Bo \equiv \rho g R^2/\sigma$, g is the acceleration of gravity).

The boundary conditions employed to complete the formulation (they are summarized in Fig. 1(*c*)) are the following. At the upper end of the tube—the inlet section—we impose a parabolic velocity profile with mean velocity $\mathcal{U}$. At the nozzle wall, the no-slip

boundary condition is prescribed. Far downstream of the nozzle (at $x=25$) we assume that the fluid adopts the velocity of the substrate, due to the effect of viscosity. Therefore we impose there a flat velocity profile given by $\mathbf{v}=\mathbf{i}$. Since the liquid-gas interface is a material surface (any mass transfer across it is assumed negligible during a time scale relevant to the deposition process), the kinematic condition applies there:

$$(\mathbf{v}-\dot{\mathbf{x}})\cdot\mathbf{n}=0 \tag{3}$$

where $\dot{\mathbf{x}}$ is the velocity at which the free surface moves ($\dot{\mathbf{x}}=\mathbf{0}$ in steady state) and $\mathbf{n}$ is the outwardly pointing (referred to the liquid phase) unit vector, normal to the boundaries of the domain (the free surface in this case). Besides, on the liquid-gas interface the surface tension forces exert a normal stress given by

$$\mathbf{n}\cdot\mathbf{T}=\kappa\mathbf{n} \tag{4}$$

with $\mathbf{T}$ here being the stress tensor (given by $\mathbf{T}\equiv-p\mathbf{I}+\boldsymbol{\tau}$; $\boldsymbol{\tau}\equiv Ca[\nabla\mathbf{v}+(\nabla\mathbf{v})^T]$ is the viscous stress tensor for a Newtonian liquid) and κ being the curvature of the interface (given by $\kappa\equiv-\nabla_S\cdot\mathbf{n}$; $\nabla_S\equiv\mathbf{I}_S\cdot\nabla$ is the surface gradient operator and $\mathbf{I}_S\equiv\mathbf{I}-\mathbf{nn}$ is the surface identity tensor). Since we consider that the surface tension is constant, no tangential/Marangoni stresses are present.

As the liquid deposits on the solid, and the gas phase is being displaced, a thread of fluid is left behind. There is a triple line where the solid-liquid-gas phases intersect each other. At the front edge, this dynamic contact line advances on the solid substrate at a speed close to V, while its speed in general diminishes as we travel along the contact line away from the front. As is well known [18], from a classical continuum view there is a discontinuity in the velocity field at a moving contact line: as an observer approaches the triple line from the liquid adjacent to the substrate, the observed velocity of the fluid equals that of the substrate, according to the adherence or no-slip condition, while if the observer approaches the contact line from the free surface, the observed velocity field possesses a horizontal component that satisfies a kinematic constraint (like that of Eq. (3)) and differs—in general—from the substrate speed. The discontinuity in the velocity field leads to a non-integrable singularity in the stress field: the force is infinite at the contact line [18]. This physically unacceptable result has been commonly circumvented by means of different approaches. The assumption of the existence of a precursor film of submicron thickness ahead of the moving contact line has been employed in Refs. [19–21]; moreover, there is supporting evidence of its existence in real systems, as reviewed in Ref. [22]. Another widely used approach to relax the singularity has been to allow some finite slip between the solid and the fluid, as in Refs. [5,15,18,23]. There is physical/theoretical support for the introduction of slip near a contact line, including surface roughness [24], molecular relaxation [25], surface energy "corrugation" [26]. Other mechanisms have been proposed to relieve the moving contact line singularity, as reviewed in Ref. [27].

Certainly the problem of dynamic wetting/dewetting is very complex and is a field of active research, and a number of theories (see Refs. [28,29]) have been proposed in recent years to explain and model the process. In this work we employed a simplified approach, the so-called Navier's slip condition, that specifies a linear relationship between the shear stress at the solid and the relative slip velocity (see arts. 327 and 331 in Ref. [30]):

$$\mathbf{n}\cdot\mathbf{T}\cdot\mathbf{t}=-\frac{Ca}{\mathcal{L}}\mathbf{t}\cdot(\mathbf{v}-\mathbf{i}) \tag{5}$$

where $\mathbf{t}$ is *any* unit vector tangent to the solid-liquid interface, the standard unit vector $\mathbf{i}$ accounts for the velocity of the substrate and $\mathcal{L}\equiv L_S/R$ is a dimensionless slip-length (L_S is its dimensional counterpart), which is a phenomenological parameter that can be interpreted as the distance down into the substrate at which the extrapolated velocity profile becomes zero. Besides, since the solid substrate is impermeable, the normal component of the velocity is zero, $\mathbf{v}\cdot\mathbf{k}=0$.

At the dynamic contact line it is necessary to specify the angle (θ) at which the free surface intersects the solid substrate, i.e., the dynamic contact angle:

$$\boldsymbol{\mu}\cdot\mathbf{k}=-\sin\theta,\quad \boldsymbol{\mu}\cdot\boldsymbol{\xi}=\cos\theta \tag{6}$$

$\boldsymbol{\mu}$ and $\boldsymbol{\xi}$ being both unit vectors normal to the contact line, the former being tangent to the free surface and the latter being tangent to the substrate (see the definition in Fig. 1(*b*)). As is well known, the dynamic contact angle changes with the velocity of the contact line [22,27,31]. Since in our continuum model we do not account for intermolecular/short-range forces, the dynamic contact angle that we prescribe is a "macroscopic" angle. Based on our own (macroscopic) measurements of θ (see Appendix A, Fig. 20), and those by others (see the reviews by Refs. [22,31]), we proposed an empirical expression for θ,

$$\theta=f(Ca\,v_{CL})\ \text{with}$$
$$f(Ca\,v_{CL})\equiv\begin{cases}[1+\tanh(k_A Ca\,v_{CL})]\,(\theta_S-\theta_0)+2\theta_0-\theta_S \\ \qquad \text{for}\ \ v_{CL}\geq 0 \\ \theta_0[1+\tanh(k_R Ca\,v_{CL})] \\ \qquad \text{for}\ \ v_{CL}<0\end{cases} \tag{7}$$

where $v_{CL}\equiv(\mathbf{v}-\mathbf{i})\cdot\boldsymbol{\xi}$ is the velocity of displacement of the contact line on the substrate, k_A is an empirical parameter that expresses how fast θ increases with $v_{CL}Ca$ (when the contact line advances, i.e., $v_{CL}>0$), and θ_S and θ_0 are also empirical parameters, indicating the saturation contact angle (for $v_{CL}\gg 0$) and the static contact angle ($v_{CL}=0$), respectively. Note that the product $v_{CL}Ca$ can be regarded as the contact line Capillary number. For $v_{CL}\ll 0$ the dynamic contact angle tends to zero, at a rate larger than the rate of approach to θ_S when $v_{CL}\gg 0$ (we employ $k_A<k_R$), which intends to model a zero-receding contact angle behavior observed in the experimental determination of θ. Further details on the measurement of θ and the values obtained for the parameters θ_0, θ_S, k_A and k_R are given in Appendix A and Table 3, as well as in Appendix B.

Finally, we need to specify initial conditions for those simulations in unsteady state. We employed two kinds of initial conditions in our model: (a) In order to obtain the first steady state solutions, we ran transient numerical experiments, as will be explained later. These transient simulations were started with the fluid at rest and a very rough estimate of the free surface shape. (b) Once we obtained steady state solutions, we carried out some transient simulations using as initial condition some of these steady state solutions (but then varying some parameters, such as the extrusion speed $\mathcal{U}$ for example).

It should be noted that, in those numerical experiments intended to obtain steady state solutions, the time-derivatives of Eqs. (1) and (3) were made equal to zero. The numerical procedures applied to the transient and steady state cases possess some differences that will be explained in Sec. 3.

2.1 The Height and Width of a Straight and Uniform Track of Fluid. In steady state, assuming that the track of fluid being deposited moves—sufficiently downstream of the nozzle—as a rigid body, and possesses a uniform cross section (A) with a circular segment shape, mass conservation requires

$$A=\pi\mathcal{U} \tag{8}$$

If the contact angle between this circular segment shaped liquid line and the solid substrate is θ_0, some simple geometrical relationships (arising from consideration of the area enclosed between a chord and an arc that meets the chord at angle θ_0) allow us to write

$$A=w^2a^2=h^2b^2 \tag{9}$$

where w is the track width, h is the track height,

$$a^2 = \frac{\theta_0 - \sin\theta_0 \cos\theta_0}{4\sin^2\theta_0} \tag{10}$$

and

$$b^2 = \frac{\theta_0 - \sin\theta_0 \cos\theta_0}{(1-\cos\theta_0)^2} \tag{11}$$

Therefore both w and h depend on $\sqrt{\mathcal{U}}$.

3 Numerical Method

The set of Eqs. (1)–(2), along with the corresponding boundary conditions specified in the previous section, must be solved in a three-dimensional domain that is unknown a priori. This represents a complex nonlinear free surface problem that requires the use of a numerical technique in order to obtain approximate solutions.

The numerical analysis of viscous free surface flows is a challenging discipline which has attracted research interest over the last decades [32,33]. The numerous methods developed over this time can be classified in different ways, but probably one of the most popular distinguishes the so called "interface capturing" and "interface tracking" methods. In the first category, typically the free surface (or more generally, the interface) moves through a fixed grid, and its position is indirectly determined by solving some auxiliary equation that accounts for the interface motion as fluids are convected. The accuracy to which the interface is "captured" depends fundamentally on the grid size. The *Volume of Fluid* [34,35], *Level-Set* [36,37] and *Diffuse-Interface* [38,39] methods belong to this category of techniques. In the second category, the domain/s over which the equations are solved coincides/e with the fluid phase/s, and the grid distorts accompanying the deformation of the fluid phase/s. The interface being "tracked" forms part of the boundaries of the domain/s. The points of the grid can either move at the velocity of the fluid (*Lagrangian* methods, [40,41]) or at an arbitrary (and conveniently defined) velocity (*Arbitrary Lagrangian-Eulerian* or ALE methods, [42–45]). Since the domain deforms, the simultaneous mesh distortion frequently becomes excessive, and the computations must be stopped and eventually resumed after a re-meshing procedure (see further details below in this section, and at the beginning of Sec. 5). However, for the same level of spatial discretization, "interface tracking" methods usually have a better accuracy than "interface capturing" methods [33].

The technique employed in this work is based on the Finite Element Method, along with a deforming-mesh/ALE scheme that allows proper tracking of the free surface motion. The numerical scheme was implemented in the framework of a commercial software, Comsol Multiphysics [46]. The ALE implementation embedded in Comsol offers a mesh updating scheme known as the Winslow method [47,48]. In this method, the following equation is solved in the fluid domain to calculate the position of the grid nodes:

$$\nabla^2 \mathbf{X} = \mathbf{0} \tag{12}$$

where $\mathbf{X}$ stands for the reference coordinates, as usual in a kinematic description. In other words, $\mathbf{X}$ can be thought as the coordinates of the mesh points in the undeformed domain; in short, the mesh coordinates. As the domain deforms, nodes that in the reference configuration were at $\mathbf{x} = \mathbf{X}$ can displace to a different position, $\mathbf{x} = \mathbf{x}(\mathbf{X}, t)$ (transient simulations), or $\mathbf{x} = \mathbf{x}(\mathbf{X})$ (steady state simulations).[2] In the former case, mesh nodes move at a velocity $\dot{\mathbf{x}} \equiv \partial\mathbf{x}/\partial t|_{\mathbf{X}}$. On the free surface, the kinematic condition (Eq. (3)) is used as a boundary condition for Eq. (12), while those parts of the boundary that are fixed preserve their original reference configuration ($\mathbf{x} = \mathbf{X}$).

As stated previously, Comsol possesses embedded capabilities to solve simultaneously Eqs. (1)–(2) and (12) along with the boundary conditions stated in the previous section, including Eqs. (3)–(6), by means of the Finite Element Method (FEM). The numerical scheme implements the classical Galerkin/FEM weighted residuals formulation for spatial discretization. The domain is tessellated into an unstructured mesh of tetrahedra. Lagrangian shape functions are employed. Since Comsol allows for the modification of the equation system to be solved, we introduced the boundary conditions of Eqs. (4)–(6) as so called natural boundary conditions, as usual in FEM [49].

After the FEM spatial discretization process is applied, either a nonlinear algebraic equation system (steady state simulations) or a nonlinear ordinary differential equation system (transient simulations) is obtained. In the latter case, Comsol employs a fully implicit, variable order, adaptive time step, finite difference scheme to discretize the equations in time and finally obtain a system of nonlinear algebraic equations. Therefore, whether a transient or a steady state case is being considered, Newton-Raphson iteration is finally used to obtain the solution, i.e., the nodal values of velocity, pressure and node position.

As was mentioned at the beginning of this section, ALE techniques are susceptible to large mesh distortions when the domain deforms. The cure in these cases is usually to apply a re-meshing step. Comsol allows one to carry out this procedure, which consists basically of four steps: (a) When the mesh distortion is large (i.e. the Comsol built-in mesh quality measure is less than 0.05), the simulation is stopped at this point. (b) Using the last solution obtained—in particular the position of the nodes situated on the boundary—the software extracts the shape of the domain and adopts it as a new reference configuration. (c) A new mesh is generated on the newly generated domain. (d) The simulation is resumed, using as initial condition the solution employed to generate the domain, projected (interpolated) into the new mesh points. As will be seen in Sec. 5, several re-meshing steps could be necessary before a steady state is achieved through successive transient simulations.

3.1 Validation of the Numerical Procedure.

In order to validate the numerical procedure adopted in this work, we compared the results obtained employing our technique with those of [15], for the analysis of the deposition of a thread of fluid on a moving substrate. We also tested the independence of the numerical results with spatial discretization, by carrying out some simulations for different mesh refinements. In Sec. 6 we address the comparison of our numerical results with experimental measurements of this process.

As was mentioned previously, the process of depositing a line of fluid on a moving substrate possesses application in areas such as printed electronics and food processing. In spite of this, it is surprising that only a small number of papers tackle the numerical analysis of this problem [15–17]. Actually, to our knowledge only the work by BAER [15] conducts a study of the influence of some of the parameters on the problem, while Refs. [16,17] only show some specific results.

All the numerical simulations of the thread deposition process shown by BAER [15] were obtained for a nozzle stand-off of $\mathcal{H} = 1.78$ and $\alpha = 0$. However, as suggested by their Fig. 6, BAER's [15] model assumes that the contact line on the nozzle exit is pinned on the internal edge, instead of the external one, as our model assumes. Alternatively, one could interpret that they neglected the finite width of the nozzle wall; in contrast to what our model does.[3]

[2] $\mathbf{x} = \mathbf{x}(\mathbf{X}, t)$ (or $\mathbf{x} = \mathbf{x}(\mathbf{X})$) can be thought as a mapping from the reference configuration to the actual configuration. The Winslow method (Eq. (12)) does not produce a conformal mapping (a mapping that preserves angles). For the 2D case, it can be shown [47] that the dependent and independent variables in Eq. (12) can be inverted to obtain $\alpha(\partial^2\mathbf{x}/\partial X^2) - 2\beta(\partial^2\mathbf{x}/\partial X \partial Y) + \gamma(\partial^2\mathbf{x}/\partial Y^2) = 0$, with $\alpha = (\partial x/\partial Y)^2 + (\partial y/\partial Y)^2$, $\beta = (\partial x/\partial X)(\partial x/\partial Y) + (\partial y/\partial X)(\partial y/\partial Y)$ and $\gamma = (\partial x/\partial X)^2 + (\partial y/\partial X)^2$.

[3] There is a subtle (but potentially significant) difference between both cases: in the former, BAER's nozzle radius is matched to our inner radius; in the latter, BAER's nozzle radius is matched to our outer radius - in that case, since our model is nondimensionalized based on inner radius, we should consider twice the stand-off ($2 \times \mathcal{H} = 3.56$) and four times the mean inlet velocity ($4 \times \mathcal{U}$) in order to conduct a proper comparison with BAER's results. We shall make the former comparison, so that no rescaling of $\mathcal{H}$ and $\mathcal{U}$ is required.

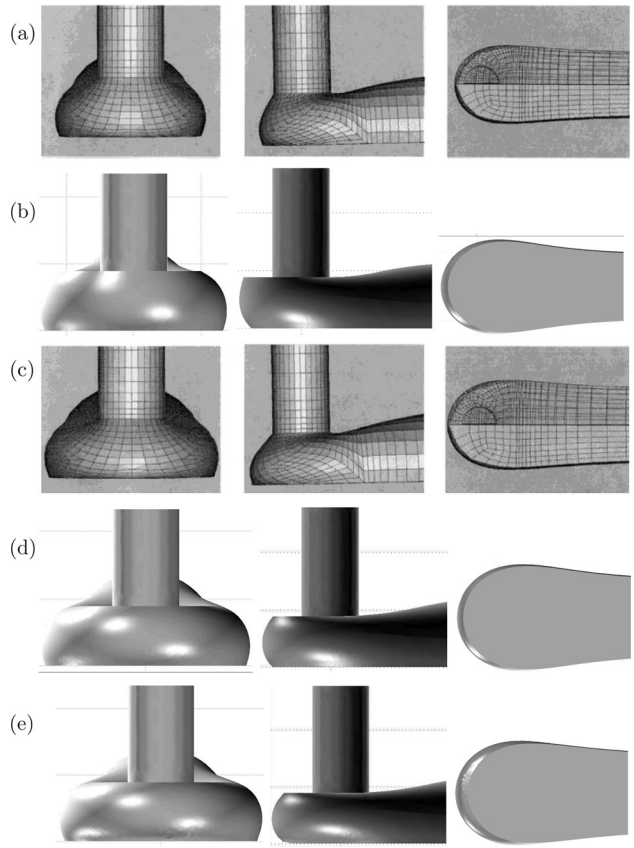

Fig. 2 The shape of the free surface viewed from different directions; comparison of the results obtained by Ref. [15] (reproduced with permission) with those obtained with our numerical technique. In all the cases $Ca = 1$, $\mathcal{H} = 1.78$, $\alpha = 0$ and $\theta_0 = 110$ deg. From top to bottom, the rows correspond to: (*a*) [15], $\theta_S = 175$ deg, $\mathcal{U} = 2.5$, steady state; (*b*) our results, $\theta_S = 110$ deg, $\mathcal{U} = 2.5$, steady state; (*c*) [15], $\theta_S = 175$ deg, $\mathcal{U} = 3.2$, steady state; (*d*) our results, $\theta_S = 110$ deg, $\mathcal{U} = 3.2$, steady state; (*e*) our results, $\theta_S = 145$ deg, $\mathcal{U} = 3.2$, transient. The remaining parameters are $\mathcal{L} = 0.5$, $La = 2.5 \times 10^{-4}$ and $Bo = 9.8 \times 10^{-3}$.

It should be pointed out that the images of the experimental process obtained both by BAER [15] and ourselves (see Fig. 10 of Ref. [15] and our Fig. 19) show that in fact the nozzle exit should be wet by the liquid being extruded (moreover, the images suggest the trailing edge could become submerged). Given that the ratio of the width of the wall to the internal radius and to the gap with the substrate are of the order of one for the problem of interest in this (and BAER's [15]) work, accounting for the nozzle wall acquires relevance, as will be seen in Fig. 2. Another important difference is that for BAER [15], the dependence of the dynamic contact angle on the contact line speed is given by $\theta = \theta_0 + (\theta_S - \theta_0)v_{CL}$, with θ_S always equal to 175 deg, independently of the capillary number. We changed our contact angle model (Eq. (7)) to that of BAER [15] for these comparisons. However, we were unable to obtain steady state solutions for the flow rates shown in that paper for $Ca = 1$ and $\theta_0 = 110$ deg, namely $\mathcal{U} = 1$, 1.6, 2.5 and 3.2 (see Fig. 7 of Ref. [15]). In order to obtain steady state solutions for $\mathcal{U} = 2.5$ and 3.2, we had to use $\theta_S = \theta_0 = 110$ deg; we could not obtain steady solutions for the smaller values of $\mathcal{U}$. When increasing θ_S to 145 deg we could only obtain a transient solution for $\mathcal{U} = 3.2$ that displays a small temporal oscillation of the contact line in the advancing front region.

The results shown by BAER [15] in their Fig. 7 consist of different views of the three dimensional liquid configuration near the deposition region. We show similar views in Fig. 2 that, as can be appreciated, display qualitative features analogous to those seen in Fig. 7 of BAER [15]. However, it is clear that the influence of considering pinning all the way to the external nozzle edge is that the

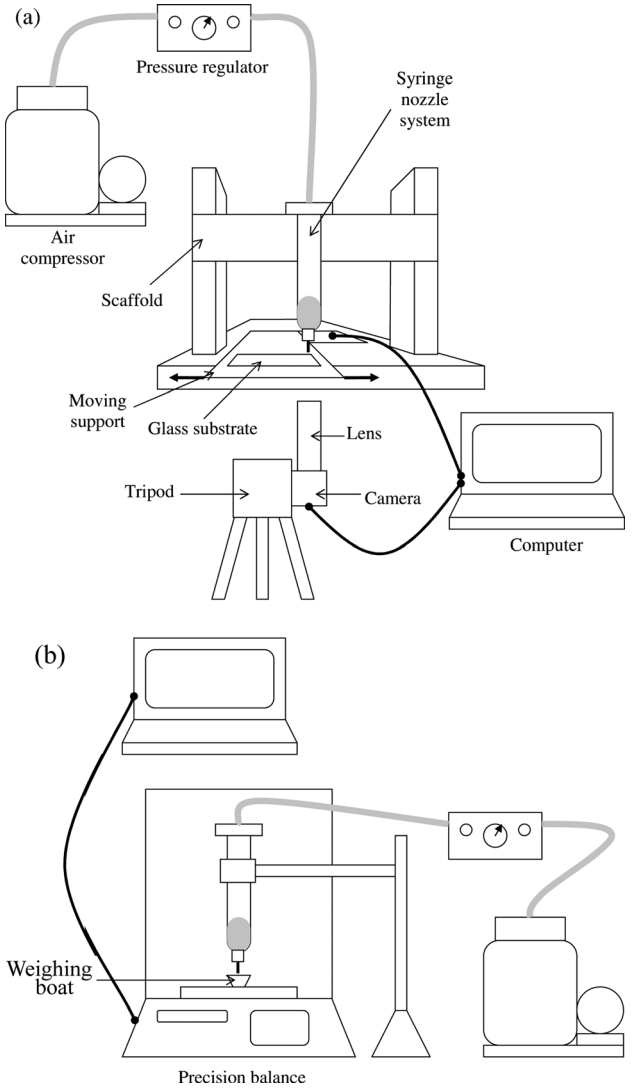

Fig. 3 Sketch of the experimental procedure: (*a*) set up employed during the deposition of the liquid line, (*b*) set up used to measure the flow rate injected through the nozzle

liquid is squeezed through the nozzle-substrate gap, resulting in a wider deposition area on the substrate. It is interesting to note that BAER's [15] results seem to show (to the naked eye) a dynamic contact angle in the advancing front of the contact line much smaller than the expected value of $\theta = \theta_S = 175$ deg (since $v_{CL} = 1$ in the leading edge in steady state). Finally, it must be pointed out that it is not clear what values BAER [15] assign to *La, Bo* and $\mathcal{L}$. In our case, we set $La = 2.5 \times 10^{-4}$, $Bo = 9.8 \times 10^{-3}$ and $\mathcal{L} = 0.5$. Given the very small value that *Bo* and *La* adopt for practical applications in the Direct-Writing of conducting tracks, the influence of these parameters on the results is negligible, as long as they remain small.

4 Description of the Experimental Methodology

The experimental measurement of the deposition of a thread of fluid consisted of two sequential steps, the recording of the deposition process itself and the measurement of the flow rate extruded through the nozzle. Figure 3 shows sketches of both experimental procedures.

During the first step, the working fluid (an epoxy flexible ink, C2050712D58 or D58 for brevity, Gwent Electronic Materials Ltd., Pontypool, United Kingdom, see Appendix A for additional details) was extruded through a nozzle of inner diameter 254 μm and outer diameter 510 μm (IJFH 560 015, Intertronics, Kidlington, UK). This nozzle was fitted to a plastic syringe (560002RB,

30cc round bottom barrel, Fisnar Inc., Fair Lawn, NJ, USA) containing the ink, which in turn was connected to a pressurised air pump (BB8-00212, Bambi Air-Compressors Ltd. Birmingham, UK) through a silicon tubing. The air pressure was regulated to a constant value during each experiment, set manually. The syringe-nozzle set was fixed to a homemade scaffold with a linear, horizontal translation capacity motor stage mounted together as operation platform (SGSP20-85 motor stage and PAT-001 power supply, Sigma Koki Co., Ltd, Japan), in such a way that the nozzle was pointing vertically downwards to the moving support. The translation speed was controlled through a PC acting on the electro-mechanical system moving the support. A glass plate was mounted horizontally on the moving support. A CCD camera (GP-MF 130, Panasonic, Japan) with an optical object lens (50X Panasonic, Japan) fitted to a camera tripod was located underneath the stage, pointing upwards, its position fixed with respect to the syringe-nozzle system, and practically aligned with it, a small horizontal offset being allowed in order to obtain pictures with the nozzle on one side of the vision field, and the deposited line of liquid running towards the opposite side. For a given set of parameters (substrate speed, nozzle-substrate distance, air pressure), the process is video recorded for a time lapse between 5 and 40 s approximately, depending on the substrate speed, long enough to allow the deposition of a liquid line between 2 and 5 cm long approximately. The pressure employed varied between 15 psi and 70 psi depending on the substrate speed, which varied between 0.5 mm s^{-1} and 5 mm s^{-1}. The applied pressure was higher at the larger the substrate speed, in order to maintain a mean injection velocity (i.e. a flow rate) of the order of the substrate speed. However, the flow rate was not controlled (in fact, the second experimental step explained below is required due to this reason).

Following each individual realization of the deposition process, the flow rate was determined by means of the following procedure. The syringe-nozzle dispensing system was situated above a small weighing boat located on a precision balance (AB265-s, Mettler Toledo, Greifensee, Switzerland), whose reading was digitally recorded in a PC, using the WinWedge32 (TalTech, Philadelphia, PA, USA) interfacing software. At a given instant of time, the fluid is pumped using the same pressure set in the immediately preceding deposition experiment. The weight of liquid poured into the container is recorded during one minute approximately, and these data are used to calculate the mass flow that, using the measured density (see Appendix A), leads to the flow rate. The procedure is repeated twice and the values are averaged.

5 Results

Practical applications of the continuous deposition of a liquid thread onto a substrate in relative motion typically require, in the first place, that the deposited line does not break into droplets, and also that the thread's dimensions are uniform and reproducible. Therefore, the identification of a steady state operating regime is of fundamental importance.

The procedure by which steady state solutions were obtained was as follows. First, we run a transient simulation using a rough guess of the free surface (basically a cuboid) as an initial configuration, which evolves in time until the mesh becomes excessively distorted. At this point, a re-meshing step is applied. The re-meshing involves extracting the flow domain shape from the last time step solution obtained, generating a new mesh on this domain and projecting the last time step solution (velocity components, pressure) onto the new mesh points. Then the numerical experiment is resumed and the system is left to evolve in time. The scheme involving *(a) resuming of transient simulation, (b) re-meshing when mesh distortion is large* is repeated until an almost steady configuration is reached. This procedure typically involves three to four iterations. We then obtain a truly steady state solution (transient terms are eliminated from the equation system) using the last transient solution as a guess for this latter simulation. After one steady state solution is obtained, the others are calculated by parametric continuation.

The results shown in this section were obtained for a fixed Capillary number, $Ca = 1.5$, a typical value in practical applications, where V is of order 10^{-3} m s^{-1}, μ is of order 10 Pa s and σ is of order 10^{-2} N m^{-1} (Appendix A contains additional details on the physical properties of a fluid used in practical applications). Given the small value of La and Bo, the influence on the results of using any particular pair of (Bo, La) is negligible, as long as these parameters remain small. Besides, as we discuss in Appendix B, the results are relatively insensitive to many of the remaining free parameters ($\mathcal{L}$, θ_0, θ_S, k_A and k_R), provided they vary around the values indicated there. Throughout subsequent subsections they will be given particular values, typical of real systems. The results shown through Secs. 5.1–5.6 were obtained using $\mathcal{L} = 0.5$, $La = 1.11 \times 10^{-4}$, $Bo = 9.8 \times 10^{-3}$, $\theta_0 = \pi/4$, $\theta_S = 3\pi/4$, $k_A = 2$ and $k_R = 13.3$. This set of parameters is obtained for a typical system where ρ is of the order of 10^3 kg m^{-3}, R is of the order of 10^{-4} m and $g = 9.8$ m s^{-2}.

5.1 Phase Diagrams. As we mentioned before, our main aim is the identification of a steady state fluid deposition regime. We already set all the parameters except $\mathcal{U}$ (the flow rate), $\mathcal{H}$ (the nozzle stand-off) and α (the nozzle tilting angle);[4] in particular, our interest is in values of $\mathcal{H}$ of the order of 1, i.e. nozzle gaps near one nozzle radius.

Following the procedure explained at the beginning of Sec. 5, we obtained steady state solutions for numerous pairs of ($\mathcal{U}$, $\mathcal{H}$)-values, for $\alpha = 0$ (a perfectly vertical nozzle) and $\alpha = \pi/9$ (a slightly downstream-ward tilted nozzle), which allowed us to build the corresponding phase diagrams. Figure 4 shows these diagrams, Fig. 4(*a*) corresponds to $\alpha = 0$ and Fig. 4(*b*) to $\alpha = \pi/9$. Small circles represent an individual steady state solution. Both graphs show that, for a particular $\mathcal{H}$, we were able to obtain steady state solutions up to a maximum and down to a minimum value of $\mathcal{U}$. The lowest $\mathcal{U}$ achievable ($\mathcal{U}_C$) were seen to be independent of the mesh refinement, while the largest $\mathcal{U}$ obtained were observed to increase as the mesh size was reduced. Therefore, we considered that the former constitute physically meaningful boundaries of the steady state regions.

An inspection of the $\mathcal{U}_C$-boundaries shown in Fig. 4 indicates that, in general, the minimum flow rate required to have a steady state regime increases as the nozzle stand-off does, and that this minimum flow rate is larger if the nozzle is slightly tilted.

In practical applications, it is commonly observed that the liquid thread being deposited on a moving substrate will tend to break up next to the nozzle exit if the flow rate is reduced excessively. Moreover, as the stand-off of the nozzle above the substrate augments, the flow rate has to be further increased to avoid the breakup of the liquid thread [12]. It is intuitive to wonder whether a relationship between this observation and the computed $\mathcal{U}_C$ boundary exists; this point will be addressed later.

Since in the tilted nozzle configuration ($\alpha = \pi/9$) the discharge of fluid is clearly favored,[5] it can be intuitively expected that when $\mathcal{H}$ is small the $\mathcal{U}_C$-boundary corresponding to $\alpha = \pi/9$ be displaced to larger values of $\mathcal{U}$, compared to $\alpha = 0$. This result suggests that, for very small stand-offs, the vertical nozzle configuration is more appropriate to deposit narrower tracks (recall that the track width decreases as the flow rate does).

As we have previously mentioned, we did not find boundaries on the right hand side (large-$\mathcal{U}$) of the steady state regions (see Fig. 4) being independent of the discretization. As stated in Sec. 2, our model assumes that the contact line is pinned to the nozzle edge, i.e., the fluid only wets the tip of the nozzle but not its lateral walls. However, in a real physical experiment, as the flow rate is increased the size of the track being deposited enlarges—both width and height, see Eqs. (8)–(11). Therefore one can expect intuitively that the contact line on the nozzle edge could eventually

[4]Upon tilt, $\mathcal{H}$ is defined to be the stand-off *averaged* over the nozzle exit.

[5]When the nozzle is vertical the fluid is squeezed more evenly through the gap with the substrate, see Fig. 5(*c*) and 5(*d*), also Fig. 11(*b*).

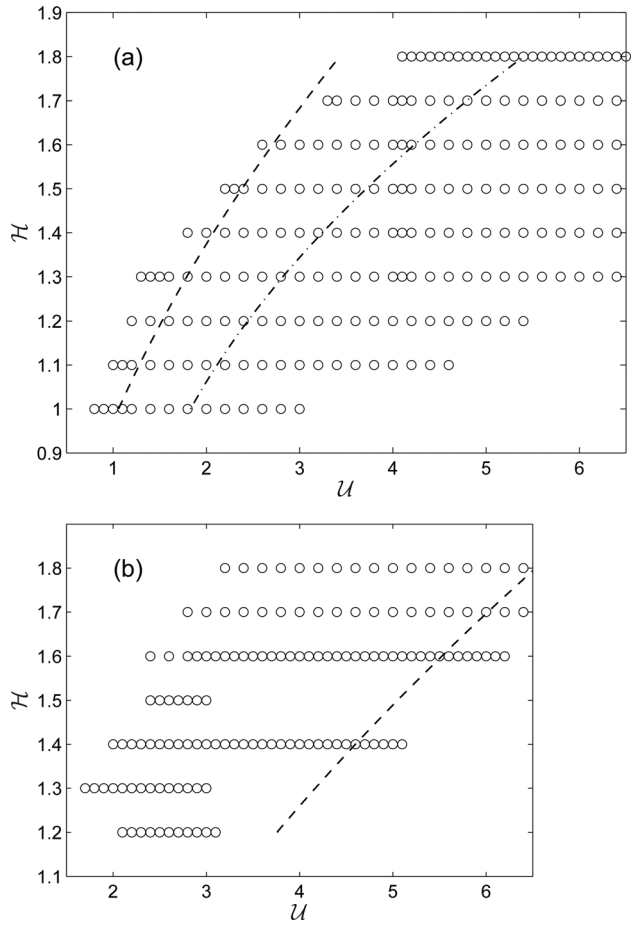

Fig. 4 Phase diagrams of steady state solutions in the ($\mathcal{U}$, $\mathcal{H}$) plane. (*a*) Vertical nozzle ($\alpha = 0$). (*b*) Tilted nozzle ($\alpha = \pi/9$). The remaining parameter values are: $Ca = 1.5$, $\mathcal{L} = 0.5$, $\theta_S = 3\pi/4$, $\theta_0 = \pi/4$, $k_A = 2$, $k_R = 13.3$, $La = 1.11 \times 10^{-4}$ and $Bo = 9.8 \times 10^{-3}$. The dashed and dot-dashed lines give different indications of the nozzle becoming submerged into the liquid being deposited; see the main text for a detailed description of the criteria defining these curves.

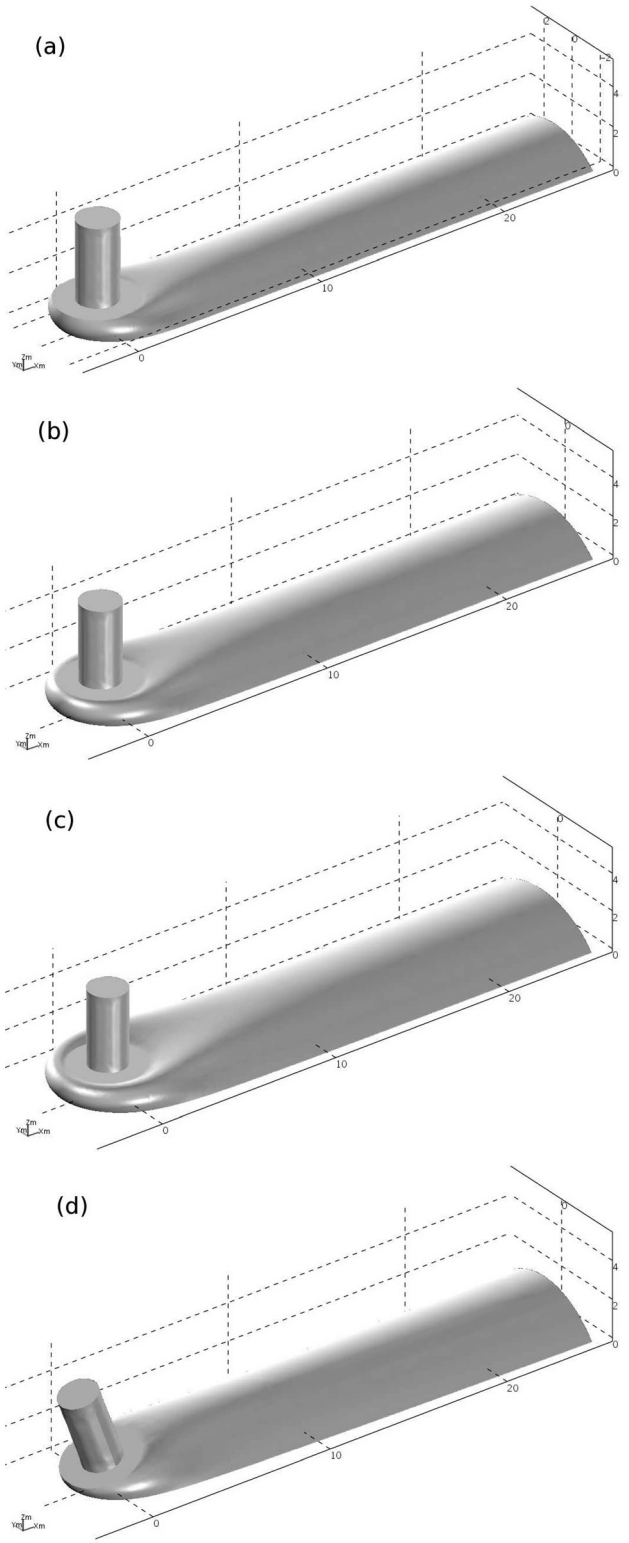

Fig. 5 Three dimensional view of some of the computed profiles of the fluid being deposited in steady state. In all the cases $Ca = 1.5$, $\mathcal{H} = 1.2$, $\mathcal{L} = 0.5$, $\theta_S = 3\pi/4$, $\theta_0 = \pi/4$, $k_A = 2$, $k_R = 13.3$, $La = 1.11 \times 10^{-4}$ and $Bo = 9.8 \times 10^{-3}$. (*a*) $\alpha = 0$ and $\mathcal{U} = 1.4$. (*b*) $\alpha = 0$ and $\mathcal{U} = 2$. (*c*) $\alpha = 0$ and $\mathcal{U} = 2.8$. (*d*) $\alpha = \pi/9$ and $\mathcal{U} = 2.8$.

de-pin from this site and the nozzle becomes submerged into the liquid. Even when it would be desirable to define criteria predicting the occurrence of this phenomenon, it is not simple to establish a rigorous condition for the de-pinning of the contact line: the "macroscopically apparent" de-pinning phenomenon actually depends on the microscopic geometry and surface properties of the nozzle edge—perfect corners do not exist physically—as well as the properties of the fluid. Therefore we will only present conditions giving an indication of the proximity of occurrence of (but not strictly determining) the nozzle immersion event.

The dashed lines seen in Fig. 4 represent the flow rate ($\mathcal{U}_{S1}$) required to have a deposited track whose height—far downstream of the nozzle—equals the maximum distance between the nozzle and the substrate ($\mathcal{H}$ for the vertical nozzle, $\mathcal{H} + 2\sin\pi/9$ for the tilted case). According to the simple expressions in Eqs. (8), (9) and (11):

$$\mathcal{U}_{S1} = \frac{(\mathcal{H} + 2\sin\alpha)^2(\theta_0 - \sin\theta_0\cos\theta_0)}{\pi(1 - \cos\theta_0)^2} \tag{13}$$

The shape of the liquid being deposited for solutions with $\mathcal{U}$ barely above $\mathcal{U}_{S1}$ has an appearance like that shown in Fig. 5(*b*). Compare it for example with Fig. 5(*a*), which corresponds to a flow rate slightly below $\mathcal{U}_{S1}$.

The dot-dashed line in Fig. 4(*a*) (note it is only shown for the vertical nozzle case) represents the minimum flow rate ($\mathcal{U}_{S2}$) required to observe an angle between the external wall of the nozzle and the free surface of the liquid equal to or less than $\pi/2$,

along the whole nozzle circumference. This means that the liquid free surface immediately adjacent to the perimeter of the nozzle tip bulges above the plane of the outlet section. To build the curve, this time we analyzed the actual numerical solutions, i.e., the computed free surface shape around the nozzle and, as can be noticed, none of the solutions examined for the tilted nozzle configuration met the criterion. Figure 5(*c*) shows the appearance of a solution for $\mathcal{U} > \mathcal{U}_{S2}$; note that, for the same flow rate, the tilted nozzle configuration does not tend to be submerged into the stream of liquid being extruded.

As can be appreciated, both criteria—the dashed lines and the dot-dashed line—indicate that the minimum flow rate required to see the nozzle "dipped" into the liquid increases as the stand-off enlarges, describing a qualitatively correct behavior. However, since the latter criterion is based on the free surface shape next to the nozzle, rather than far downstream (see Fig. 5), we consider it a more accurate estimation. Figure 4(*a*) shows that the values of $\mathcal{U}_{S1}$ (dashed line) are always smaller—within the range of $\mathcal{H}$ analyzed—than those of $\mathcal{U}_{S2}$ (dot-dashed line). On the other hand, comparing the dashed curves corresponding to $\alpha = 0$ and $\alpha = \pi/9$ we can observe that the flow rate required in the latter case is considerably larger ($(1 + 2\mathcal{H}^{-1} \sin \pi/9)^2$ times larger) than in the former. This is a purely geometrical effect, since for the same mean stand-off ($\mathcal{H}$), the trailing edge of the tilted nozzle tip possesses a gap with the substrate larger than $\mathcal{H}$.

5.2 The Stability of the Steady State Solutions. In the last subsection we showed phase diagrams of steady state solutions in the ($\mathcal{U}$, $\mathcal{H}$) plane, for a perfectly vertical nozzle ($\alpha = 0$) and for one that is tilted ($\alpha = \pi/9$). However, the determination of a steady state parameter regime is usually not enough for practical applications: establishing the stability of these solutions is also an important issue.

In order to determine the stability of the steady state solutions, the approach followed by Ref. [50] could be employed, which consists of solving a generalized eigenvalue problem that arises from the linearization of the Finite Element equation system. This procedure involves the so-called Jacobian and mass matrices of the Finite Element scheme. However, we do not have access to these matrices because the commercial simulation software we employ does not provide them. In view of these limitations we followed an approximate approach to test the stability of the solutions, in which we perturbed the steady state solution and observed the time evolution of the system.

The procedure that we followed to analyze the stability of any particular steady state solution consisted of starting a transient simulation using as initial condition the (steady) solution being tested, but setting $\mathcal{U} = 0$ during the first 0.5 units of dimensionless time, after which we restore the original value of $\mathcal{U}$. We continue following the time evolution of the liquid being deposited, typically until $t = 30$. If the original liquid configuration is (approximately) recovered at the end of this simulation, we run an additional steady state simulation using the last solution of the transient simulation as a guess for the Newton's loop. If a converged solution is obtained in this last simulation, the steady state is catalogued as stable; otherwise it is named unstable.

Because of the large number of steady state solutions we obtained, it was impractical to test the stability of all of them. Therefore, we analyzed only those solutions lying on the left hand side ($\mathcal{U}_C$) boundaries of the steady state regions. The numerical experiments carried out determined that these solutions are stable under a finite flow rate perturbation, both for the vertical and tilted nozzle cases.

In the context of coating processes (particularly curtain and slot coating, see Ref. [13]), there is a well-known stability issue at low flow rates (or more specifically when the ratio $\mathcal{U}$ between flow speed and substrate speed is low), usually referred to as the air-entrainment problem: the contact line on the front meniscus loses stability, tends to displace downstream and air enters into the gap between the die and the web/substrate (slot coating) or destroys the impinging curtain (curtain coating). In spite of the obvious geometrical differences (these processes produce both plane film coatings, while the problem of interest here generates a thread-shaped deposit), there could be some relationship between the $\mathcal{U}_C$-boundary found in this paper and the air-entrainment phenomenon, especially considering the contact line behavior illustrated in Figs. 7–8.

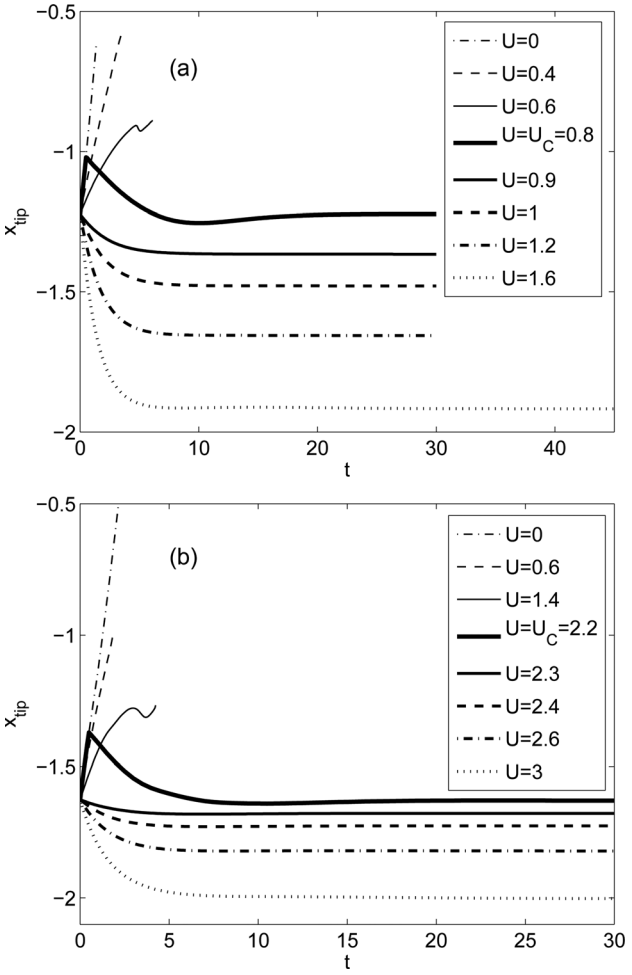

Fig. 6 The time evolution of the tip of the contact line of the deposited track, for several values of $\mathcal{U}$. (*a*) $\mathcal{H} = 1$, (*b*) $\mathcal{H} = 1.5$. The remaining parameters are: $\alpha = 0$, $Ca = 1.5$, $L = 0.5$, $\theta_S = 3\pi/4$, $\theta_0 = \pi/4$, $k_A = 2$, $k_R = 13.3$, $La = 1.11 \times 10^{-4}$ and $Bo = 9.8 \times 10^{-3}$.

5.3 The Transient Evolution of the System for Flow Rates Increasingly away from the $\mathcal{U}_C$-Boundaries of the Steady State Regions. In the last subsection, we perturbed steady state solutions—lying on the boundaries of the steady state regions—and analyzed their subsequent transient evolution. In this subsection we also observe time evolutions that start from steady state configurations corresponding to solutions lying on the boundary of the steady region, though now we impose a flow rate ($\mathcal{U}$) either less or larger than the critical value ($\mathcal{U}_C$).

In Fig. 6 we observe the transient evolution of the x-coordinate of the front tip of the contact line (x_{tip}) for several values of $\mathcal{U}$ and $\alpha = 0$; the upper graph corresponds to $\mathcal{H} = 1$ and the lower graph to $\mathcal{H} = 1.5$. In all the cases, the tip evolves initially from the same position ($x_{tip,C}$, the steady state value) to either downstream ($x_{tip} > x_{tip,C}$) or upstream ($x_{tip} < x_{tip,C}$) locations, depending on whether the flow rate imposed is smaller or larger than $\mathcal{U}_C$, respectively. The thickest solid curves are drawn for reference: they correspond to the critical flow rate ($\mathcal{U}_C$). These curves show the time evolution during the stability tests (Sec. 5.2) carried out on these

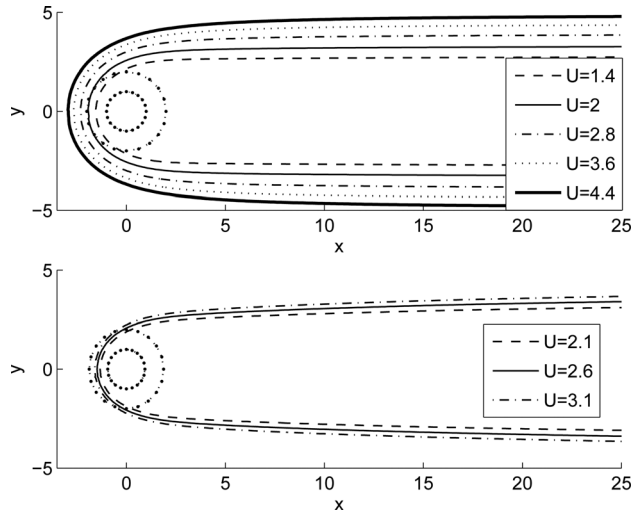

Fig. 7 The shape of the contact line of the deposited track, for several values of $\mathcal{U}$. Vertical nozzle above ($\alpha = 0$), tilted nozzle below ($\alpha = \pi/9$). The remaining parameters are: $\mathcal{H} = 1.2$, $Ca = 1.5$, $\mathcal{L} = 0.5$, $\theta_S = 3\pi/4$, $\theta_0 = \pi/4$, $k_A = 2$, $k_R = 13.3$, $La = 1.11 \times 10^{-4}$ and $Bo = 9.8 \times 10^{-3}$.

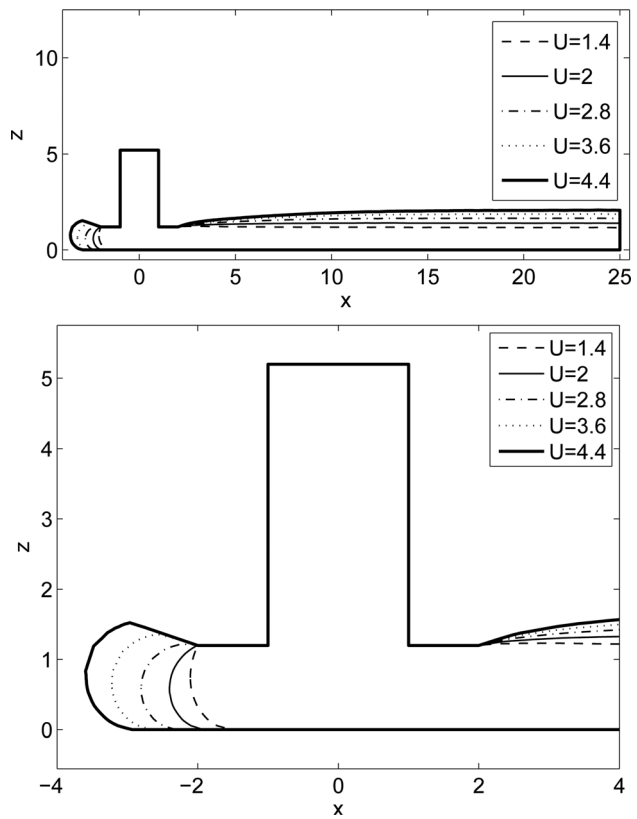

Fig. 8 Longitudinal section ($y = 0$) of the profile of the fluid deposited on the substrate, for several values of $\mathcal{U}$. The remaining parameters are: $\alpha = 0$, $\mathcal{H} = 1.2$, $Ca = 1.5$, $\mathcal{L} = 0.5$, $\theta_S = 3\pi/4$, $\theta_0 = \pi/4$, $k_A = 2$, $k_R = 13.3$, $La = 1.11 \times 10^{-4}$ and $Bo = 9.8 \times 10^{-3}$. Complete view above, close-up of the nozzle region below. Note that the nozzle inner surface has unit radius, but the nozzle outer surface (the outer surface is not drawn explicitly) has twice that radius.

cases, lying on the $\mathcal{U}_C$-boundaries. Following the perturbation in the flow rate, the tip of the contact line undergoes a strongly damped slow oscillation, recovering finally (as expected) the equilibrium position, $x_{tip} = x_{tip,C}$.

In both graphs of Fig. 6 we observe a clear behavior when $\mathcal{U} > \mathcal{U}_C$: the system attains the steady state configuration corresponding to the imposed flow rate ($\mathcal{U}$). During the early stages of the evolution, the tip approaches exponentially to its final position and by $t \sim 10$ the tip is within 0.01 units of $x_{tip,C}$.

On the other hand, when $\mathcal{U} < \mathcal{U}_C$ (note these flow rates are outside the steady state region) we observe a different type of evolution: the tip undergoes a transient evolution, after which the numerical scheme stops converging. The lack of convergence is seen to occur at earlier times as the flow rate is further diminished. In fact, experimental observations [12] indicate that there exists a critical (nonzero) flow rate below which the liquid thread being deposited tends to breakup (obviously for $\mathcal{U} = 0$ the continuity of the liquid line will be interrupted).

5.4 Influence of $\mathcal{U}$. A variation of the parameter $\mathcal{U}$ alone can be immediately interpreted as a change in the flow rate. There is, however, another interpretation: a scaling of the physical dimensions of the system (as long as the influence of inertia (La) and gravity (Bo) remains almost negligible) also leads to a change in $\mathcal{U}$.

As intuition indicates, we have already seen (e.g. see Sec. 2.1 and Fig. 5) that both the width and the height of the deposited track enlarge as $\mathcal{U}$ increases. Nonetheless, we chose some of the solutions of Fig. 4 (for a fixed stand-off, $\mathcal{H} = 1.2$) in order to explore in depth the influence of $\mathcal{U}$. Fig. 7 shows vertical views of the contour of the deposited tracks (i.e. the contact line) for $\mathcal{H} = 1.2$, with $1.4 \leq \mathcal{U} \leq 4.4$ for the vertical nozzle (top) and $2.1 \leq \mathcal{U} \leq 3.1$ for the tilted one (bottom). For reference, the inner and outer nozzle walls are represented by dotted lines.

Again, both for $\alpha = 0$ and $\pi/9$, we immediately see that, as $\mathcal{U}$ increases, the track becomes wider and the deposition area below the nozzle becomes broader. Besides, the width of the deposited line of liquid increases progressively downstream of the nozzle, tending to the final value given by Eqs. (8)–(11). Table 1 shows the track width downstream of the nozzle, both the theoretical calculation and the numerical prediction at the end of the domain ($x = 25$). The approach to the theoretical value is less close for the tilted nozzle configuration, and for the larger values of $\mathcal{U}$. A final approach is not observed due to the finite length (along the x-axis) of the domain. The widening of the track along the x-axis (as elements of fluid move downstream of the nozzle) is due to a spreading of the liquid that takes place as the cross section (constant x) of the fluid changes from the shape of the liquid emerging from the nozzle to the circular segment shape that is finally expected for a static line of liquid.

In Fig. 8 we show longitudinal sections (taken in the plane $y = 0$) of the flow domain, which allow one to see the profile of the liquid free surface. The sections correspond to the same cases analyzed in Fig. 7. The graphs clearly show the tendency of the liquid to bulge around the nozzle and of the nozzle to become submerged into the stream of fluid, as the flow rate is increased.

Table 1 The width of the deposited track. The theoretical values are calculated using Eqs. (8)–(11), while the numerical predictions are measured at $x = 25$. The remaining parameters are: $\mathcal{H} = 1.2$, $Ca = 1.5$, $\mathcal{L} = 0.5$, $\theta_S = 3\pi/4$, $\theta_0 = \pi/4$, $k_A = 2$, $k_R = 13.3$, $La = 1.11 \times 10^{-4}$ and $Bo = 9.8 \times 10^{-3}$.

α	0 (vertical nozzle)				
$\mathcal{U}$	1.4	2	2.8	3.6	4.4
Theoretical width	5.55	6.64	7.85	8.90	9.84
Numerical width	5.47	6.52	7.70	8.72	9.60
α	$\pi/9$ (tilted nozzle)				
$\mathcal{U}$	2.1	2.6	3.1		
Theoretical width	6.80	7.57	8.26		
Numerical width	6.21	6.80	7.33		

On the contrary, for the smallest flow rates, bulging is not so pronounced and the advancing front of the contact line tends to be located below the nozzle (see also Fig. 7, upper plot). They also display the process by which the cross section of the track evolves along the x-axis to adopt the circular segment shape far downstream.

At this point it is relevant to point out one aspect of our model. We are employing a constant value of viscosity, representative of the process taking place in the deposition region. However, this value possibly might not be representative of the process occurring downstream of the nozzle, where the track recently deposited is adopting its final configuration. Shear rates in this region could be considerably smaller compared to those typical of the deposition region which, for the characteristic shear-thinning behavior displayed by inks employed in practice, implies that the fluid should be expected to be more viscous in the track. This in turn would lead to a slowing down of the process where the track cross section becomes circular. In Appendix C we show a few numerical experiments addressing the influence of the shear-thinning on the track shape, which indicate that this influence is negligible.

5.5 Influence of $\mathcal{H}$. The modification of $\mathcal{H}$ for a fixed set of the remaining parameters can be mostly interpreted as variation in the nozzle-substrate distance. However, it could also mean a change in the size of the nozzle (as long as the importance of inertia and gravity remain still small) while the mean inflow velocity and the rest of the conditions remain unchanged.

The influence of $\mathcal{H}$ on some aspects of the problem was partly analyzed in previous subsections, but in this subsection we study particularly the effect of this parameter on the shape of the deposited line of liquid in a region extending down to a little above ten (inner) nozzle diameters downstream of the nozzle tip.

We again chose steady solutions from the charts of Fig. 4, for a fixed value of $\mathcal{U}$ ($\mathcal{U}=2.8$ for $\alpha=0$ and $\mathcal{U}=3$ for $\alpha=\pi/9$), with $\mathcal{H}$ between 1 and 1.6 in the former case and between 1.2 and 1.6 in the latter. Figure 9 shows vertical views (the plane $z=0$) of the edges of the track (the contact line), the upper graph corresponding to the vertical nozzle and the lower graph to the tilted case. Figure 10 displays longitudinal sections (the plane $y=0$) of the flow domain for the cases corresponding to a vertical nozzle of Fig. 9.

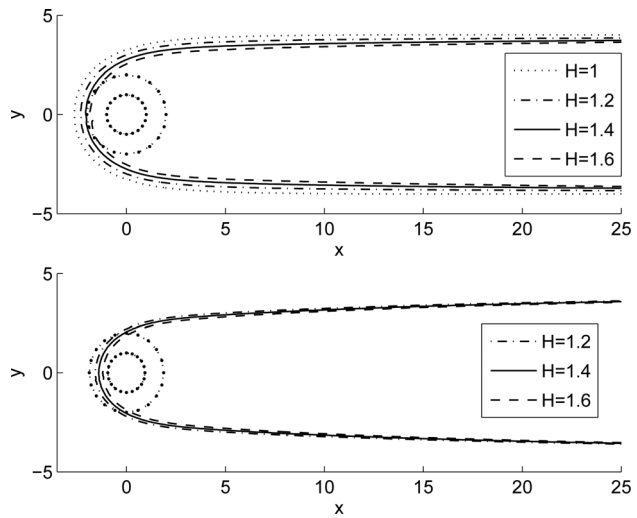

Fig. 9 The shape of the contact line of the deposited track, for several values of $\mathcal{H}$. Vertical nozzle above ($\alpha=0$, $\mathcal{U}=2.8$), tilted nozzle below ($\alpha=\pi/9$, $\mathcal{U}=3$). The remaining parameters are: $Ca=1.5$, $\mathcal{L}=0.5$, $\theta_S=3\pi/4$, $\theta_0=\pi/4$, $k_A=2$, $k_R=13.3$, $La=1.11\times10^{-4}$ and $Bo=9.8\times10^{-3}$.

Table 2 The width of the deposited track. The theoretical values are calculated using Eqs. (8)–(11), while the numerical predictions are measured at $x=25$. In addition $\mathcal{U}=2.8$ for the vertical nozzle case and $\mathcal{U}=3$ for the tilted nozzle case. The remaining parameters are: $Ca=1.5$, $\mathcal{L}=0.5$, $\theta_S=3\pi/4$, $\theta_0=\pi/4$, $k_A=2$, $k_R=13.3$, $La=1.11\times10^{-4}$ and $Bo=9.8\times10^{-3}$.

α	0 (vertical nozzle)			
$\mathcal{H}$	1	1.2	1.4	1.6
Theoretical width		7.85		
Numerical width	8.03	7.70	7.46	7.29
α	$\pi/9$ (tilted nozzle)			
$\mathcal{H}$	1.2	1.4	1.6	
Theoretical width		8.13		
Numerical width	7.23	7.15	7.08	

We can appreciate in Fig. 9 that, as the stand-off increases, the width of the track and the deposition area below the nozzle both reduce. In particular, it is clear that the leading edge of the contact line becomes closer to the nozzle outlet (the inner nozzle wall in the graph).

Besides, as Fig. 9 and Table 2 show, the width of the tracks far downstream from the nozzle tends to the same value, as expected since $\mathcal{U}$ is constant. However, there is an interesting case for the vertical nozzle configuration: while the remaining cases approach the theoretical value (see Table 2) with a width at $x=25$ slightly smaller, the case corresponding to $\alpha=0$ and $\mathcal{H}=1$ displays a track width slightly above the theoretical prediction. A closer look at Fig. 9 indicates that track width remains almost constant for $x>7$ approximately. According to our empirical model of the dynamic contact angle (Eq. (7)), the contact line is allowed to advance but it can (almost) not recede, which explains the behavior observed in this particular case.

Figure 10 shows also the tendency of the front tip of the contact line (x_{tip}) to be situated further upstream of the nozzle as $\mathcal{H}$ is reduced, and of the front meniscus to bulge farther ahead of the nozzle. Far downstream of the deposition region, the height of the liquid line of the different cases tends to equate, as expected since the flow rate is the same.

5.6 Influence of α. In previous subsections it has been shown that the tilting angle (α) has different effects on the deposition of a liquid line. In particular (see Figs. 7 and 9) the wet area in the deposition region (the region surrounding the nozzle) has a more tapered shape, and the width of liquid line at a short distance downstream of the nozzle is narrower, compared to the vertical nozzle case. Figure 11 reinforces these findings. These results correspond to a flow rate of $\mathcal{U}=2.8$ and a stand-off of $\mathcal{H}=1.2$. The width of the track predicted by Eqs. (8)–(11) is 7.85; the computed track widths approach to this value as the distance (along the x-axis) away from the nozzle increases. At $x=25$ the widths are 7.70 and 7.02, for the vertical and tilted nozzle cases respectively.

On the other hand, the longitudinal sections of Fig. 12 show the clear diminishing of the bulging of the fluid around the nozzle as it is extruded, when the nozzle is tilted. This effect in turn translates into a contact line situated closer to the nozzle exit (and in particular larger values of x_{tip}). Another consequence of the nozzle tilting is that the height of the track cross section is considerably larger near the nozzle than for $\alpha=0$, which in turn produces a narrower track in this region. Then, as the distance downstream of the nozzle (or the x-coordinate) increases, the cross sections of both cases tend to equate and attain the circular segment shape, due to the effect of the surface tension.

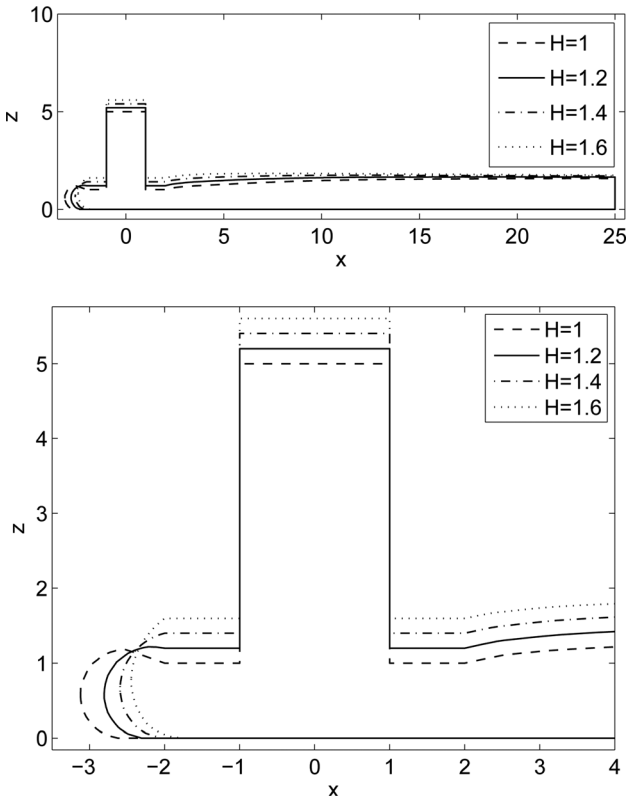

Fig. 10 Longitudinal section ($y=0$) of the profile of the fluid deposited on the substrate, for several values of $\mathcal{H}$. The remaining parameters are: $\alpha=0$, $\mathcal{U}=2.8$, $Ca=1.5$, $\mathcal{L}=0.5$, $\theta_S=3\pi/4$, $\theta_0=\pi/4$, $k_A=2$, $k_R=13.3$, $La=1.11\times10^{-4}$ and $Bo=9.8\times10^{-3}$. Complete view above, close-up of the nozzle region below.

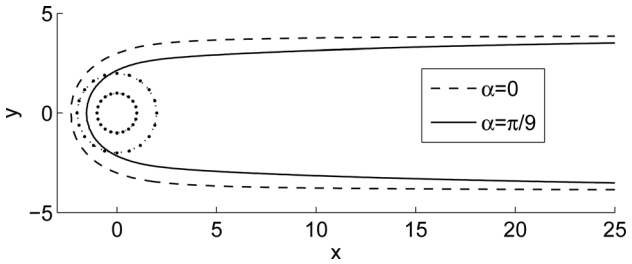

Fig. 11 The shape of the contact line of the deposited track, for two values of α. The remaining parameters are: $\mathcal{U}=2.8$, $\mathcal{H}=1.2$, $Ca=1.5$, $\mathcal{L}=0.5$, $\theta_S=3\pi/4$, $\theta_0=\pi/4$, $k_A=2$, $k_R=13.3$, $La=1.11\times10^{-4}$ and $Bo=9.8\times10^{-3}$. Note that the nozzle projections illustrated in dotted lines correspond to the case $\alpha=0$, but the one corresponding to $\alpha=\pi/9$ is very similar.

6 Comparison with Experiments

In order to evaluate the capacity of the model to predict or reproduce the behavior of the actual system, we carried out a comparison between the numerical simulations and our experimental measurements, for a limited number of cases. Both the experimental setup and procedure were previously explained in Sec. 4.

We recorded videos of the liquid deposition conducted in the laboratory. We were able to video record the process from below the substrate since we deposited the fluid on glass plates. Figures 13 and 15 show images corresponding to one instant of time of the actual videos, on top of which the respective numerical predictions of the track borders (the contact line) were superposed. In order to have a reference to superpose properly the picture of the track and the numerical results, we also video recorded

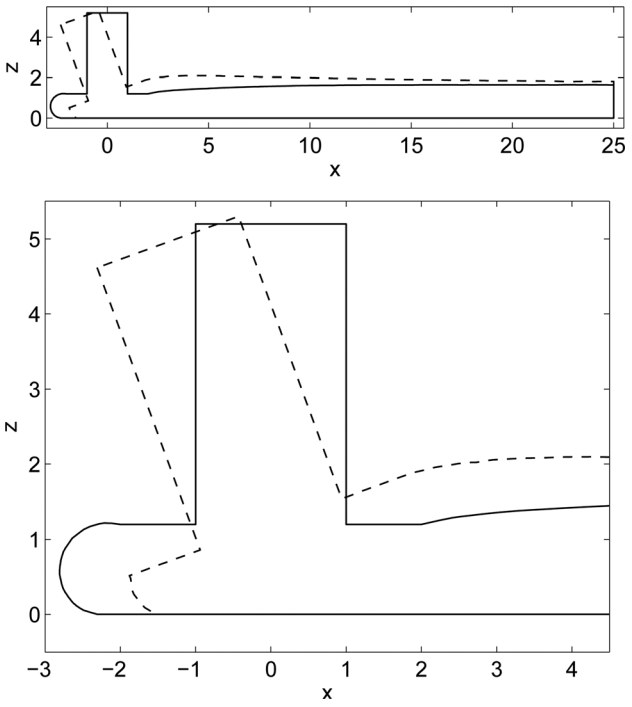

Fig. 12 Longitudinal section ($y=0$) of the profile of the fluid deposited on the substrate, for two values of α. The remaining parameters are: $\mathcal{H}=1.2$, $\mathcal{U}=2.8$, $Ca=1.5$, $\mathcal{L}=0.5$, $\theta_S=3\pi/4$, $\theta_0=\pi/4$, $k_A=2$, $k_R=13.3$, $La=1.11\times10^{-4}$ and $Bo=9.8\times10^{-3}$. Complete view above, close-up of the nozzle region below.

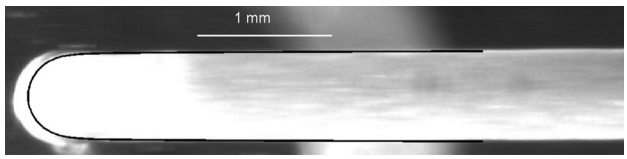

Fig. 13 The shape of the deposited track viewed from below the substrate: an image of the actual deposition process is superposed on the numerical prediction shown as a black solid curve. In this case $Ca=1.68$ and $\mathcal{U}=1.2$. The remaining parameters are: $\alpha=0$, $\mathcal{H}=1$, $\mathcal{L}=0.5$, $\theta_S=135$ deg, $\theta_0=39.1$ deg, $k_A=5.9$, $k_R=11.9$, $La=1.08\times10^{-4}$ and $Bo=1.49\times10^{-2}$.

the nozzle alone before starting to pump fluid through it. The nozzle was aligned vertically ($\alpha=0$) and the tip was situated approximately one nozzle radius above the substrate ($\mathcal{H}=1$). Besides, we employed the following set of parameters to conduct the numerical experiments: $\mathcal{L}=0.5$, $\theta_S=135$ deg, $\theta_0=39.1$ deg, $k_A=5.9$, $k_R=11.9$, $La=1.08\times10^{-4}$ and $Bo=1.49\times10^{-2}$. Both Ca and $\mathcal{U}$ (essentially the substrate speed and the flow rate) changed from one experiment to the other.

Besides, in Figs. 14 and 16 we show close-ups of the track profiles of Figs. 13 and 15 respectively, without the superposed numerical predictions, along with views from below the substrate of the respective tri-dimensional liquid shapes, calculated numerically, that allow one to appreciate both the wet area on the substrate and the liquid free surface bulging above the plane $z=0$.

Figure 13 corresponds to $Ca=1.68$ and $\mathcal{U}=1.2$. A very good agreement is seen between the profile of the track being deposited and the numerical prediction, except in the region immediately around the nozzle. We suspect that the external part of the white profile seen in the advancing front region (at the left in the image) is not actually liquid in contact with the substrate, but rather the free surface of the liquid located between the substrate and the nozzle. An inspection of the pictures in Fig. 14 reveals a qualitative resemblance between both images that seems to support the

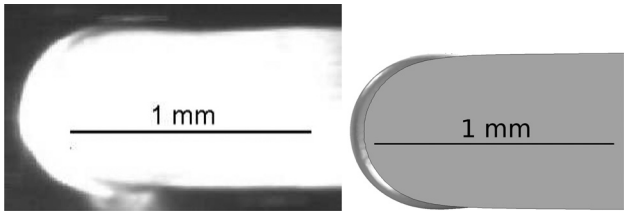

Fig. 14 A close-up of the deposition region viewed from below the substrate. Left: picture of the actual process. Right: image obtained from the numerical results. In this case $Ca = 1.68$ and $\mathcal{U} = 1.2$. The remaining parameters are: $\alpha = 0$, $\mathcal{H} = 1$, $\mathcal{L} = 0.5$, $\theta_S = 135$ deg, $\theta_0 = 39.1$ deg, $k_A = 5.9$, $k_R = 11.9$, $La = 1.08 \times 10^{-4}$ and $Bo = 1.49 \times 10^{-2}$.

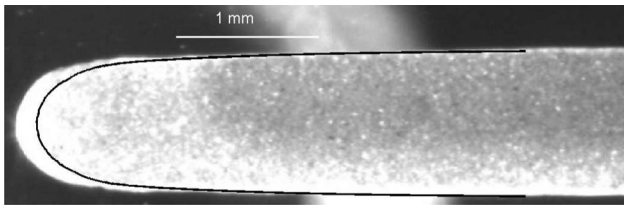

Fig. 15 The shape of the deposited track viewed from below the substrate: an image of the actual deposition process is superposed on the numerical prediction shown as a black solid curve. In this case $Ca = 0.168$ and $\mathcal{U} = 2.5$. The remaining parameters are: $\alpha = 0$, $\mathcal{H} = 1$, $\mathcal{L} = 0.5$, $\theta_S = 135$ deg, $\theta_0 = 39.1$ deg, $k_A = 5.9$, $k_R = 11.9$, $La = 1.08 \times 10^{-4}$ and $Bo = 1.49 \times 10^{-2}$.

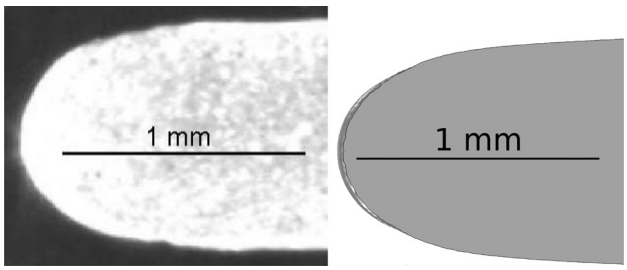

Fig. 16 A close-up of the deposition region viewed from below the substrate. Left: picture of the actual process. Right: image obtained from the numerical results. In this case $Ca = 0.168$ and $\mathcal{U} = 2.5$. The remaining parameters are: $\alpha = 0$, $\mathcal{H} = 1$, $\mathcal{L} = 0.5$, $\theta_S = 135$ deg, $\theta_0 = 39.1$ deg, $k_A = 5.9$, $k_R = 11.9$, $La = 1.08 \times 10^{-4}$ and $Bo = 1.49 \times 10^{-2}$.

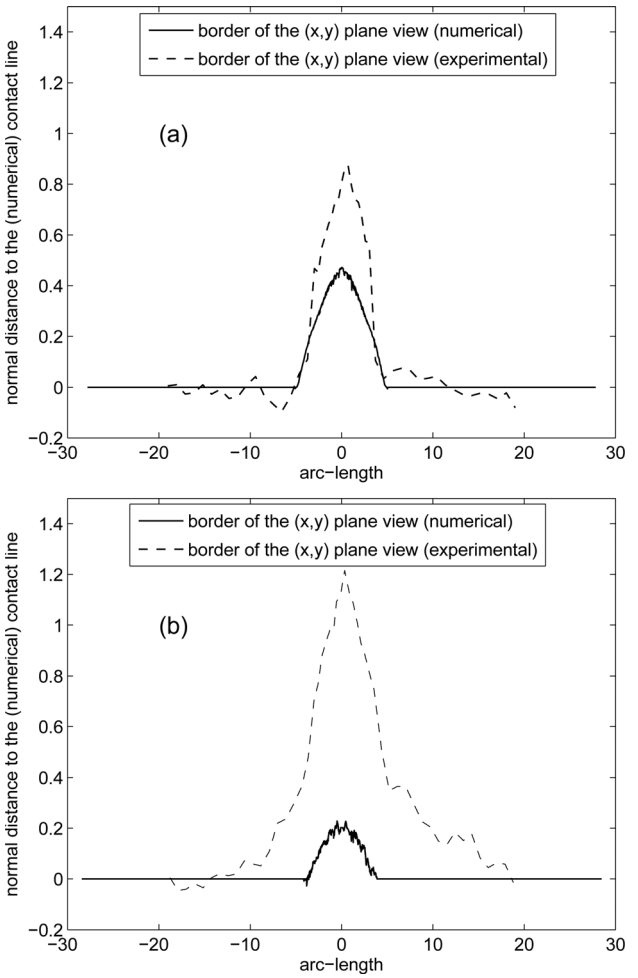

Fig. 17 The normal distance to the contact line computed numerically, as a function of the arc- length along the contact line. The 0-value corresponds to the front tip. Magnitudes are dimensionless. (*a*) $Ca = 1.68$ and $\mathcal{U} = 1.2$. (*b*) $Ca = 0.168$ and $\mathcal{U} = 2.5$. The remaining parameters are: $\alpha = 0$, $\mathcal{H} = 1$, $\mathcal{L} = 0.5$, $\theta_S = 135$ deg, $\theta_0 = 39.1$ deg, $k_A = 5.9$, $k_R = 11.9$, $La = 1.08 \times 10^{-4}$ and $Bo = 1.49 \times 10^{-2}$.

argument presented above, and the lateral views of the actual process shown in Fig. 19 (and also in Fig. 10 of Ref. [15]) also seem to reinforce it.

The results displayed in Fig. 15 ($Ca = 0.168$ and $\mathcal{U} = 2.5$) show that, except in the nozzle region, the agreement is also very good. As in the previous case (Fig. 13), we observe the largest differences in the front meniscus of the deposition area.

Since the picture of Fig. 15 is not very clear near the white edges in the deposition area, we again examined the computed three-dimensional shape of the liquid, viewed from below the substrate. As we can observe in Fig. 16 (corresponding to the case shown in Fig. 15, $Ca = 0.168$ and $\mathcal{U} = 2.5$), this time the free surface is predicted to protrude only a very small distance in front of the contact line.

In order to explore this argument further, we calculated the normal distance to the numerical contact line, both from the borders of the image recorded experimentally and from the projected (onto the (x, y) plane) shape of the free surface obtained numerically. We plotted (in Fig. 17) the results corresponding to the cases of Figs. 14 and 16, as a function of the arc length measured from the front tip of the contact line. Magnitudes are dimensionless, positive distances indicate points "outside" the numerical contact line, and *vice versa*. It is clear from these results, and also from the observation of Figs. 14 and 16, that the differences between the numerical and experimental results (see Figs. 13 and 15) cannot be explained only by the bulging of the free surface around the nozzle.

There are many other possible causes for the observed differences, including: (a) the nozzle stand off was set before each experimental determination using a metal sheet of calibrated thickness, but considering the small dimensions of our system (of the order of one hundred microns), there could be some uncertainty in its value, especially when considering any potential secular tilting in the displacing substrate;[6] (b) the wetting/contact line behavior of the system might not be properly modeled: for more sophisticated theories, see Ref. [28]; (c) the fluid used in the experiments is also known to have some visco-elastic characteristics, that could potentially produce a swelling phenomenon at the nozzle exit,

[6]From the videos taken from the side, we estimate a gap variation around 25 microns in a typical running distance of 5 cm, which represents an uncertainty of 25% approximately for a 100 microns gap. This variation in gap is consistent with a secular tilting around 0.03 deg.

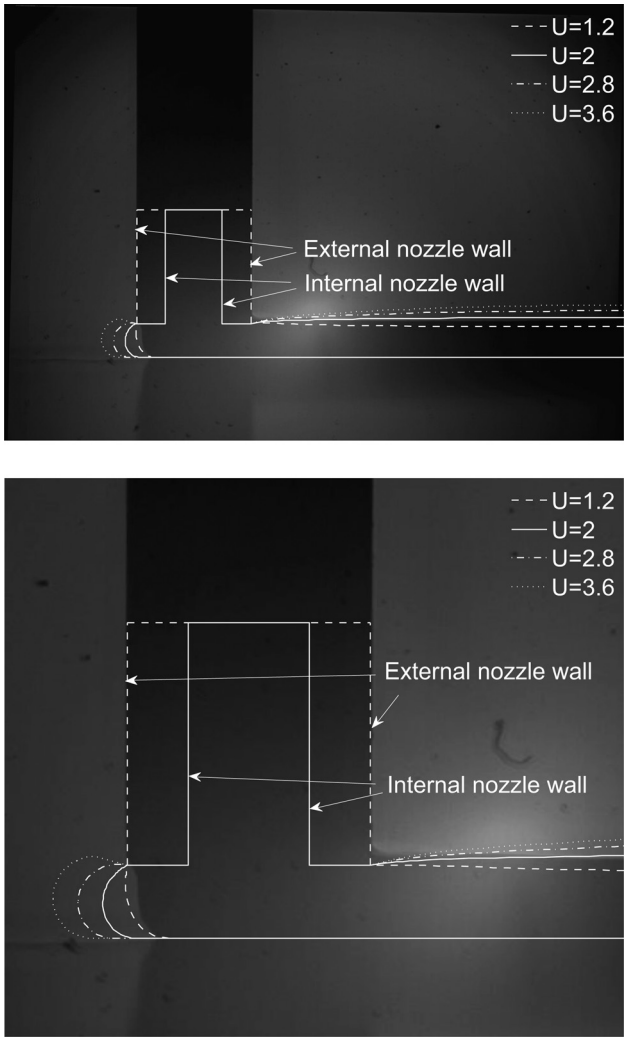

Fig. 18 Comparison of a side-view of the liquid thread being deposited with longitudinal sections ($y=0$) of the computed profiles, for several values of $\mathcal{U}$. The remaining parameters are: $\alpha=0$, $\mathcal{H}=1.2$, $Ca=1.5$, $\mathcal{L}=0.5$, $\theta_S=3\pi/4$, $\theta_0=\pi/4$, $k_A=2$, $k_R=13.3$, $La=1.11\times10^{-4}$ and $Bo=9.8\times10^{-3}$. Note that the external nozzle wall is depicted only for clarity, but does not form part of the computational domain in the simulations.

where the fluid is being deposited on the substrate (recall that our fluid model is Newtonian); (d) part of the lateral walls of the nozzle tip could have been wet by the fluid, either because of a large flow rate (e.g. Fig. 15) or because of insufficient cleaning before the experiment.

It is interesting to note that in the former case (Fig. 13) the edges of the track (the contact line) are relatively parallel, while in the latter case (Fig. 15) the width of the track increases as we move away downstream the nozzle. In both cases, the numerical results correctly reproduce the behavior of the actual physical process, although the predicted shape of the contact line in the advancing front region tends to be more tapered than the experimentally observed shape, in the latter case (Fig. 15).

We also compared our numerical results with images of the process recorded from the side. However, since in these cases the flow rate was not measured (data were gathered primarily for determination of contact angles; see Appendix A), a systematic comparison procedure was not possible. Only for illustration purposes, we show one of these comparisons in Fig. 18. In this case, the substrate was moving towards the right in the image, at a speed of 5 mm s^{-1}. Overlaid are different profiles computed for sets of parameters similar to the experimental ones, and similar to those already illustrated in Fig. 8. The numerical result that best agrees with the experiment is $\mathcal{U}=1.2$, although the agreement is not especially good. In the experiment, the contact line on the nozzle does not seem to be pinned along the whole nozzle edge, as imposed in the simulations. On the advancing side (left) the contact line looks slightly downstream the nozzle tip, and on the trailing side (right) the fluid seems to wet part of the lateral (vertical) walls of the nozzle.

7 Final Remarks and Conclusions

We have studied numerically the deposition of a liquid thread on a moving substrate, with special interest in cases where the capillary number is near unity and the dispensing nozzle is located around one nozzle radius above the substrate, as well as typical values of Direct-Write technologies applied to printed electronics. The study required us to perform both transient and steady state simulations of the 3D process.

We found a region of steady state solutions in terms of the flow rate and nozzle stand-off parameters for two different nozzle configurations: in one case the nozzle is pointing vertically to the substrate, in the other it is pointing slightly towards the direction of substrate motion. The capillary number was set to a typical value of 1.5 in these numerical experiments. Although the remaining parameters were also fixed, we showed that their influence is not important on the results, provided they vary within certain limits.

The phase diagrams show the existence of a minimum flow rate below which we could not obtain steady state solutions. This minimum flow rate in general increases as the nozzle stand-off does, and is larger when the nozzle is tilted. This suggests that the vertical nozzle configuration seems to be more appropriate for relatively low flow rate operations when the nozzle stand-off is around or less than one nozzle radius. The solutions on these $\mathcal{U}_C$-boundaries were seen to be stable under a flow rate perturbation. For the vertical nozzle case, we also provide an indication of the minimum flow rate required to submerge the nozzle tip into the stream of fluid being deposited; as the substrate-nozzle distance increases, a larger flow rate is needed. Since we did not observe the "submerged nozzle" condition in the tilted nozzle case, this configuration seems to be a good measure to avoid the nozzle being dipped into the fluid.

Additional transient simulations seem to confirm, on one hand, that the solutions *within* the steady state region are also stable and, on the other, that steady state solutions cannot be attained for flow rates below $\mathcal{U}_C$. Limitations in the numerical technique prevented us from exploring in depth the mechanism of liquid breakup that exists when the flow rate is too small or nil.

Parametric studies of steady state solutions show that the width of the liquid line being printed decreases as we either diminish $\mathcal{U}$, augment $\mathcal{H}$ or increase α, although only the former retains influence far downstream.

We also carried out experimental measurements of the actual deposition process for a limited number of cases and compared them with the corresponding numerical predictions. Specifically, we analyzed the shape of the track being deposited on the substrate. The agreement obtained was, in general, good, although there are some relatively important differences in the region closer to the nozzle, particularly near the advancing front meniscus. The reason for these differences is not clear, and cannot be explained solely by a lack of clarity of the pictures taken during the experiments.

The study of this problem can be extended in several directions. Similar phase diagrams to those of Fig. 4 could also be obtained for different values of the Capillary number, which would be of great interest since this is the main parameter in determining the working deposition regime. We have obtained a limited number of results (not shown in this paper) for smaller capillary numbers, reaching values down to $Ca=5\times10^{-4}$.

It would also be interesting to extend the phase diagrams for larger values of $\mathcal{H}$, in order to determine the flow rate regime appropriate for these stand-offs. For large $\mathcal{H}$ different "meandering" behaviors of the depositing liquid thread have been observed [10,11].

Besides, it would be interesting to examine aspects related to the liquid breakup mechanism. The breakup could not only occur near the nozzle due to an excessively small flow rate, but it could also take place in the already deposited thread of fluid due to a capillary/contact line instability [5–8].

Although shear-thinning effects seem to be negligible for the parameters of interest in this paper (see Appendix C), they could become important for other parameter regimes, for smaller capillary numbers for instance. Furthermore, more complex rheological characteristics (such as visco-elasticity) are being ignored and future models could account for this kind of behavior of the fluid.

Some geometrical characteristics of the system could also be explored, as for example, the nozzle tilting angle and direction, or the (nozzle wall thickness)/(internal nozzle radius) ratio.

Acknowledgment

To the DW-EASY consortium for providing us with valuable information and materials related to the direct writing of liquid tracks, and to the Technology Strategy Board. S. Ubal acknowledges support from EPSRC contract EP/D062128/1 and Consejo Nacional de Investigaciones Científicas y Técnicas (CONICET). Thanks is also given for permission to produce Fig. 10 of Ref. [15], "A Finite Element Method for Free Surface Flows of Incompressible Fluids in Three Dimensions. Part II. Dynamic Wetting Lines," International Journal for Numerical Methods in Fluids, John Wiley & Sons, Ltd.

Appendix A: Experimental Methods for Determining the Physico-Chemical Properties of the System

We study the deposition of a line of fluid on a moving substrate mainly motivated by printed electronics applications. The dimensionless parameters employed within the paper are based on realistic operating conditions and actual fluid properties. One fluid of interest in these applications is a type of flexible ink which contains 58% silver metal (both silver nanoparticles and silver flakes) and epoxy resin (C2050712D58 or D58 for brevity, Gwent Electronic Materials Ltd., Pontypool, United Kingdom).

We determined experimentally most of the physico-chemical properties of this ink relevant to this paper, including the density, the surface tension, and the static and dynamic contact angles when deposited on glass substrates. On the other hand, the viscosity was measured by Printed Electronics Ltd.

The density of the ink (ρ) was calculated measuring the weight of a known volume of ink. The procedure was repeated 3 times, and the result was $\rho = 2.0 \pm 0.1$ g cm^{-3}.

The surface tension of the fluid (σ) was determined using the pendant drop method. The procedure was repeated three times, and the value determined was $\sigma = 20.5 \pm 1.4$ mN m^{-1}.

The static contact angle (θ_0) of the ink on a glass substrate was measured video recording a sessile droplet of fluid. The procedure was repeated three times, and the measured value was $\theta_0 = 39.1 \pm 1.9$ deg.

Regarding the dependence of dynamic contact angle (θ) on the contact line capillary number ($v_{CL}Ca$, see the definition in Sec. 2 after Eq. (7)), the procedure to measure it required the use of the same experimental setup described in Sec. 4 and employed to obtain the pictures shown in Sec. 6. However, this time the images were taken from the side of the deposited line instead from beneath, resulting in a view similar to those displayed in Figs. 8 and 10 and 12.

The contact angle was measured at the front tip of the contact line, where (in steady state) the contact line speed equals that of the substrate (since the position of the contact line remains fixed, relative to the nozzle). Therefore, the contact line capillary number is equivalent to the capillary number of the experimental determination. The capillary number in the experiments was calculated using a viscosity of $\mu = 6.9$ Pa s (see below) and a surface tension of $\sigma = 20.5$ mN m^{-1}. We carried out measurements for four different substrate speeds, namely 0.5 mm s^{-1}, 1 mm s^{-1}, 2 mm s^{-1} and 5 mm s^{-1}. The images obtained (see Fig. 19 for some sample cases) were processed with the software Matlab, where the profile of the free surface in the front meniscus was extracted and the angle with the substrate was determined. About 15 images per substrate speed were analyzed and the values were averaged. The results can be seen in Fig. 20, along with a curve fitted to the data,

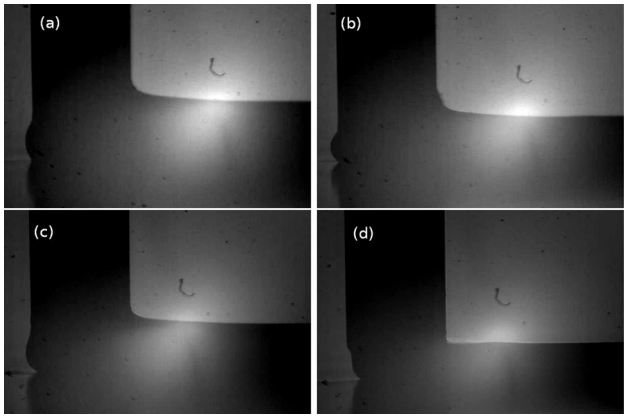

Fig. 19 Snapshots of the deposition process recorded from the side, employed to measure the dynamic contact angle: (*a*) $V = 0.5$ mm s^{-1}, (*b*) $V = 1$ mm s^{-1}, (*c*) $V = 2$ mm s^{-1} and (*d*) $V = 5$ mm s^{-1}

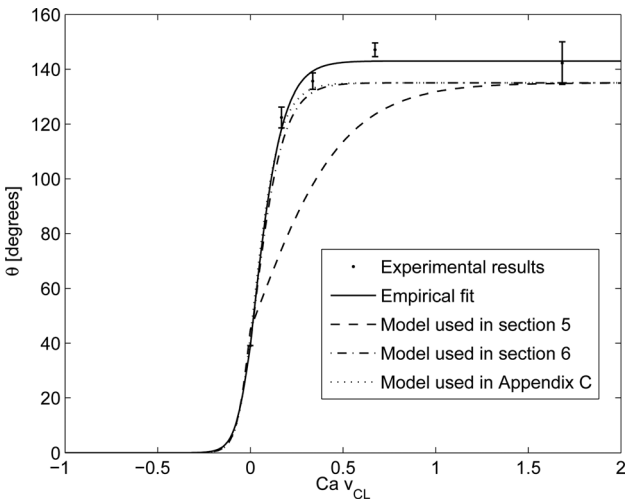

Fig. 20 The dynamic contact angle as a function of the contact line speed

Table 3 The parameters of the empirical formula of Eq. (7). The values displayed are both the experimentally extracted ones and those employed in the numerical results shown in this paper, more amenable for the numerical calculations.

Parameter	k_A	k_R	θ_0	θ_S
Best fit	5.9	11.9	39.1 deg	143 deg
Used in §5	2	13.3	45 deg	135 deg
Used in §6	5.9	11.9	39.1 deg	135 deg
Used in Appendix C	6.7	13.3	42.5 deg	135 deg

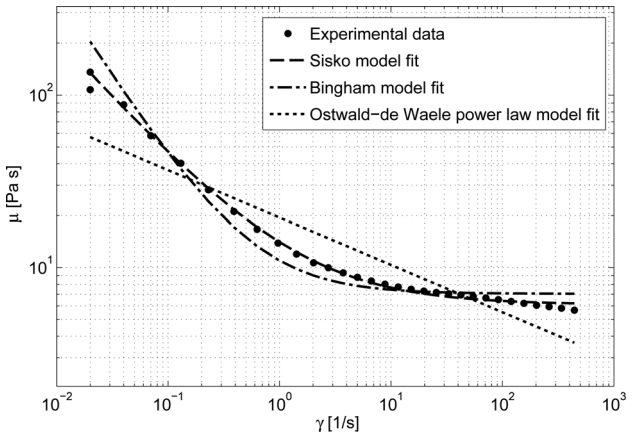

Fig. 21 The viscosity of the D58 ink as a function of the shear rate, along with some shear-thinning fluid models

Table 4 The parameters of the empirical formula of Eq. (A1), corresponding to different models, best fitting the experimental data of Fig. 21

Parameter	μ_∞ (Pa s)	m (Pa s^n)	n
Sisko model	6.1	8	0.29
Bingham model	7.1	3.9	0
Power law model	0	19.5	0.73

employing the empirical formula of Eq. (7). The parameters of the curve are shown in Table 3. Since the employment of this set of parameters produced some (small) numerical oscillations in the free surface, we instead used a different set of values that avoided those numerical oscillations (see Fig. 20 and Table 3), after having determined that the results obtained are not strongly influenced by this change (see also Appendix B for additional details).

Finally, as we said before, Printed Electronics Ltd. provided the rheological tests of the D58 ink, undertaken at a temperature of 25 °C. Figure 21 shows the viscosity (μ) as a function of the (dimensional) shear rate ($\dot{\gamma}$), along with the curve fittings corresponding to some common fluid models. The experimental curve displays, in gross terms, two different behaviors: for $0.02\ s^{-1} < \dot{\gamma} < 2\ s^{-1}$ the fluid could be modeled as a power law fluid with some given parameters, while for $2\ s^{-1} < \dot{\gamma} < 400\ s^{-1}$ the power law parameters seem to change. For reference, the shear rate in the nozzle region is of the order of tens of s^{-1}. However, the Sisko fluid model [51] fits very well to the behavior observed for the range of values of $\dot{\gamma}$ studied. This model states that the viscosity depends on the shear rate according to the following expression

$$\mu = \mu_\infty + m\dot{\gamma}^{n-1} \tag{A1}$$

where μ_∞, m and n are empirical fluid parameters, μ_∞ being the asymptotic value to which the viscosity of the fluid tends for large shear rates, m is the so-called "consistency" of the fluid and n is a dimensionless constant smaller than unity for shear-thinning fluids (and larger than unity for shear-thickening fluids). The Newtonian fluid behavior is recovered by either setting $m=0$ or $n=1$ in Eq. (A1). The fluid parameters extracted for various different fluid models can be seen in Table 4.

In view of the Newtonian behavior assumed in our model (see Sec. 2), the experimental measurements referred to above, and the range of shear rates expected in the deposition region, we chose (as stated earlier) a viscosity of 6.9 Pa s for the numerical experiments carried out in this paper.

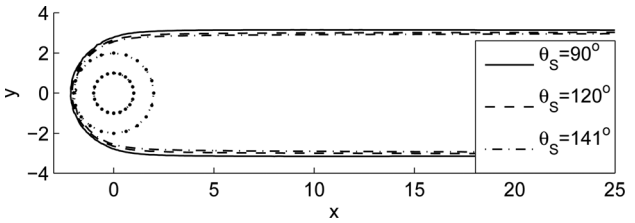

Fig. 22 The shape of the contact line of the deposited track, for three values of θ_S. The remaining parameters are: $\theta_0 = 39.1$ deg, $k_A = 6.7$, $k_R = 13.3$, $La = 1.11 \times 10^{-4}$, $Bo = 9.8 \times 10^{-3}$, $\alpha = 0$, $Ca = 1.5$, $\mathcal{H} = 1$, $\mathcal{U} = 1.6$ and $\mathcal{L} = 0.5$.

Appendix B: Sensitivity to the Contact Line Parameters

The values given to the dimensionless parameters in Sec. 5 correspond to realistic operating conditions and actual material properties used in practical applications. The experimental measurement of the physico-chemical properties of the materials has an inherent uncertainty. Besides this, the measurement of the dynamic contact angle determines, in particular, values having an "apparent" nature, since the measurement is carried out at a specific macroscopic length scale. Therefore, even though most of the simulations were done for a specific set of contact line parameters (see Eq. (7) and also Table 3), it is important to analyze the sensitivity of the results to variations of these parameters.

The numerical experiments carried out to observe the influence[7] of k_A, θ_0 and θ_S on the results were obtained for $\alpha = 0$, $\mathcal{H} = 1$, $\mathcal{U} = 1.6$, $La = 1.11 \times 10^{-4}$, $Bo = 9.8 \times 10^{-3}$, $k_R = 13.3$ and $\mathcal{L} = 0.5$. In the first instance we varied θ_0 using $k_A = 6.7$ and $\theta_S = 135$ deg. The results (data are not presented here) were very similar, in fact no appreciable difference can be observed in the shape of the deposited tracks of fluid.

We then varied k_A, using $\theta_0 = \pi/4$ and $\theta_S = 3\pi/4$. In this case (again data are not presented here) the influence is a little more pronounced, but still very small. The width of the track tends to be slightly smaller (especially just downstream of the nozzle) as k_A increases (i.e. as θ varies faster with $v_{CL}Ca$), which is a sensible behavior, but track widths tend to equate farther downstream.

Finally, Fig. 22 shows the effect of varying θ_S between 90 deg and 141 deg, using $\theta_0 = 39.1$ deg and $k_A = 6.7$. Also in this case we observe that the influence of this contact angle parameter is not too large. As θ_S increases we can note a small narrowing of the deposited line, in particular just downstream of the nozzle, which is also a behavior that could be expected, since the "saturation" contact angle (that observed near the leading meniscus) is larger.

In summary, we can conclude that modifying the contact angle parameters within the range considered in this appendix does not produce large deviations in the shape of the deposited line of liquid. In particular, we can infer from these results that using $\theta_S = 3\pi/4$, $\theta_0 = \pi/4$ and $k_A = 2$ instead of the experimentally obtained values $\theta_S = 143$ deg, $\theta_0 = 39.1$ deg and $k_A = 6.7$, should not introduce significant quantitative differences, with the benefit that using the former set of parameters is more amenable for our numerical simulations.

Appendix C: The Effect of the Shear-Thinning Behavior of the Ink on the Track Width

We have already pointed out earlier in this paper that actual inks employed in the direct writing of lines of fluid on a substrate display typically non-Newtonian behaviors, most visibly shear-thinning (see Appendix A). For simplicity, nevertheless, the numerical model employed to obtain the results shown in Sec. 5

[7]The influence of varying k_R was deemed less important, as any reasonably large k_R value in Eq. (7) gives near-zero receding contact angles, in line with experimental observations.

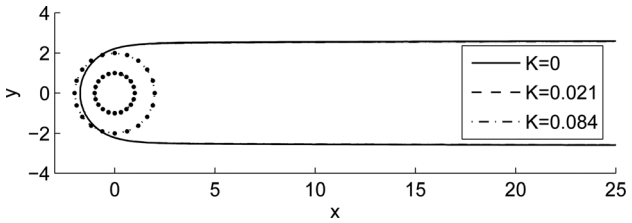

Fig. 23 The shape of the deposited track for three values of K. The remaining parameters are $n = 0.29$, $Ca = 1.33$, $\mathcal{U} = 1.2$, $\mathcal{H} = 1$, $\alpha = 0$, $\mathcal{L} = 0.5$, $\theta_S = 135$ deg, $\theta_0 = 42.5$ deg, $k_A = 6.7$, $k_R = 13.3$, $La = 1.85 \times 10^{-4}$ and $Bo = 1.6 \times 10^{-2}$.

assumes the liquid being Newtonian. The calculation of the dimensionless parameters (namely the Capillary number) was based on a viscosity value representative of the shear rates expected in the deposition region (tens of s^{-1}), but viscosity in the already deposited track (where shear rates are smaller) could be considerably larger than this. Therefore, in this appendix we include a shear thinning model Eq. (A1), the so-called Sisko model (see Ref. [51]) in our numerical scheme, to study the influence of this effect. The dimensionless expression for the momentum conservation is now

$$La\ Ca\left(\frac{\partial \mathbf{v}}{\partial t} + \mathbf{v}\cdot\nabla\mathbf{v}\right) = \frac{1}{Ca}\nabla\cdot\mathbf{T} - \frac{Bo}{Ca}\mathbf{k} \tag{C1}$$

where now $Ca \equiv \mu_\infty V/\sigma$, and $\mathbf{T}$ is the total stress tensor, given by

$$\mathbf{T} \equiv -p\mathbf{I} + 2Ca\,\eta\mathbf{D} \tag{C2}$$

with $\mathbf{D} \equiv 1/2[\nabla\mathbf{v} + (\nabla\mathbf{v})^T]$ being the strain rate tensor and η a dimensionless viscosity defined by (see also Eq. (A1))

$$\eta \equiv \frac{\mu}{\mu_\infty} = 1 + K\dot{\Gamma}^{n-1} \tag{C3}$$

where $K \equiv (m/\mu_\infty)(V/R)^{n-1}$ is a new dimensionless parameter, along of course with n (recall that the definition of Ca also changed). The dimensionless shear rate ($\dot{\Gamma}$) of Eq. (C3) is defined by $\dot{\Gamma} \equiv R\dot{\gamma}/V \equiv (2\mathbf{D}:\mathbf{D})^{1/2}$. The introduction of the Sisko model also affects Navier's slip condition, which now reads

$$\mathbf{n}\cdot\mathbf{T}\cdot\mathbf{t} = -\eta\frac{Ca}{\mathcal{L}}\mathbf{t}\cdot(\mathbf{v}-\mathbf{i}) \tag{C4}$$

where the slip-length ($\mathcal{L}$, in dimensionless form) preserves the same meaning as in Eq. (5). In Eq. (C4), $\mathbf{n}$ is the outwardly pointing unit normal (i.e. pointing downwardly into the substrate here) and $\mathbf{i}$ represents the dimensionless substrate velocity, which equals the x-axis standard unit vector.

In order to examine the influence of the shear thinning behavior, we obtained a few results for different values of the parameter K defined before, while $n = 0.29$, $Ca = 1.33$, $\mathcal{U} = 1.2$, $\mathcal{H} = 1$, $\alpha = 0$, $\mathcal{L} = 0.5$, $\theta_S = 135$ deg, $\theta_0 = 42.5$ deg, $k_A = 6.7$, $k_R = 13.3$, $La = 1.85 \times 10^{-4}$ and $Bo = 1.6 \times 10^{-2}$, which constitutes a set of parameters representative of realistic operating conditions. As we can observe in Fig. 23, the tracks corresponding to the different values of K are practically identical ($K = 8.4 \times 10^{-2}$ represents the behavior of the D58 ink shown in Fig. 21, and $K = 0$ corresponds to the Newtonian case, with $\mu = \mu_\infty$). If one observes the viscosity of the fluid (for the largest K case) in the deposition region, from the leading meniscus down to four nozzle radii downstream of the nozzle axis ($x = 4$, this result is not shown here), we can see an increase of only 30% (i.e. $\eta = 1.3$). This implies that the local Capillary number ($\eta\,Ca$) in this region would rise up to 1.73. The reason for this relatively small viscosity increment is that the shear rate regime in the deposition region lies in the flat region of the curve of Fig. 21 for $\dot{\gamma} > 0.5\ s^{-1}$. Assuming for simplicity that the dimensionless shear rate distribution is roughly the same for different values of Ca, we can speculate that a two-fold decrease of the order of magnitude of the substrate velocity (and therefore of Ca), with a consequent $2(1-n)$-fold increase of the order of magnitude of K, should be required to notice some shear thinning effect on the track width. Additionally, we would also need to analyze the effect on the tilted nozzle case.

References

[1] Piqué, A., and Chrisey, D. B., 2002, *Direct-Write Technologies for Rapid Prototyping Applications: Sensors, Electronics, and Integrated Power Sources*, Academic Press, San Diego.
[2] Calvert, P., 2001, "Inkjet Printing for Materials and Devices," Chem. Mater., **13**, pp. 3299–3305.
[3] Lewis, J. A., and Gratson, G. M., 2004, "Direct Writing in Three Dimensions," Mater. Today, **7**, pp. 32–39.
[4] Lewis, J. A., 2006, "Direct Ink Writing of 3D Functional Materials," Adv. Funct. Mater., **16**, pp. 2193–2204.
[5] Davis, S. H., 1980, "Moving Contact Lines and Rivulet Instabilities. Part 1. The Static Rivulet," J. Fluid Mech., **98**, pp. 225–242.
[6] Sekimoto, K., Oguma, R., and Kawasaki, K., 1987, "Morphological Stability Analysis of Partial Wetting," Ann. Phys., **176**, pp. 359–392.
[7] Schiaffino, S., and Sonin, A. A., 1997, "Formation and Stability of Liquid and Molten Beads on a Solid Surface," J. Fluid Mech., **343**, pp. 95–110.
[8] González, A. G., Diez, J., Gratton, R., and Gomba, J., 2007, "Rupture of a Fluid Strip Under Partial Wetting," EPL,**77**, 44001.
[9] Duineveld, P. C., 2003, "The Stability of Ink-Jet Printed Lines of Liquid with Zero Receding Contact Angle on a Homogeneous Substrate," J. Fluid Mech., **477**, pp. 175–200.
[10] Chiu-Webster, S., and Lister, J. R., 2006, "The Fall of a Viscous Thread onto a Moving Surface: A Fluid-Mechanical Sewing Machine," J. Fluid Mech., **569**, pp. 89–111.
[11] Morris, S. W., Dawes, J. H. P., Ribe, N. M., and Lister, J. R., 2008, "Meandering Instability of a Viscous Thread," Phys. Rev. E, **77**, p. 066218.
[12] Xu, B., 2010, "Inkjet Printing of Silver for Direct Write Applications," Ph. D. thesis, The University of Manchester, School of Materials, UK.
[13] Weinstein, S. J., and Ruschak, K. J., 2004, "Coating Flows," Annu. Rev. Fluid Mech., **36**, pp. 29–53.
[14] Carvalho, M. S., and Kheshgi, H. S., 2000, "Low-Flow Limit in Slot Coating: Theory and Experiments," AIChE J., **46**, pp. 1907–1917.
[15] Baer, T. A., Cairncross, R. A., Schunk, P. R., Rao, R. R., and Sackinger, P. A., 2000, "A Finite Element Method for Free Surface Flows of Incompressible Fluids in Three Dimensions. Part II. Dynamic Wetting Lines," Int. J. Numer. Methods Fluids, **33**, pp. 405–427.
[16] Fan, H., Lu, Y., Stump, A., Reed, S. T., Baer, T., Schunk, R., Perez-Luna, V., Lopez, G. P., and Brinker, C. J., 2000, "Rapid Prototyping of Patterned Functional Nanostructures," Nature, **405**, pp. 56–60.
[17] Fan, H., Reed, S., Baer, T., Schunk, R. P., López, G., and Brinker, C. J., 2001, "Hierarchically Structured Functional Porous Silica and Composite Produced by Evaporation-Induced Self-Assembly," Microporous Mesoporous Mater., **44**, pp. 625–637.
[18] Huh, C., and Scriven, L. E., 1971, "Hydrodynamic Model of Steady Movement of a Solid/Liquid/Fluid Contact Line," J. Colloid Interface Sci., **35**, pp. 85–101.
[19] Diez, J. A., Kondic, L., and Bertozzi, A., 2001, "Global Models for Moving Contact Lines," Phys. Rev. E., **63**, p. 011208.
[20] Gaskell, P. H., Jimack, P. K., Sellier, M., and Thompson, H. M., 2004, "Efficient and Accurate Time Adaptive Multigrid Simulations of Droplet Spreading," Int. J. Numer. Methods Fluids, **45**, pp. 1161–1186.
[21] Maurya, R. S., Sundararajan, T., and Das, S. K., 2009, "Development of a PLIC-VOF Method for the Dynamic Simulation of Entry Region Flow in a Laminar Falling Film," Int. J. Comput. Fluid Dyn., **23**, pp. 391–400.
[22] de Gennes, P. G., 1985, "Wetting: Statics and Dynamics," Rev. Mod. Phys., **57**, pp. 827–863.
[23] Hocking, L. M., 1977, "A Moving Fluid Interface. Part 2. The Removal of the Force Singularity by a Slip Flow," J. Fluid Mech., **79**, pp. 209–229.
[24] Hocking, L. M., 1976, "A Moving Fluid Interface on a Rough Surface," J. Fluid Mech., **76**, pp. 801–817.
[25] Huh, C., and Mason, S. G., 1977, "The Steady Movement of a Liquid Meniscus in a Capillary Tube," J. Fluid Mech., **81**, pp. 401–419.
[26] Thompson, P. A., and Troian, S. M., 1997, "A General Boundary Condition for Liquid Flow at Solid Surfaces," Nature, **389**, pp. 360–362.
[27] Bonn, D., Eggers, J., Indekeu, J., Meunier, J., and Rolley, E., 2009, "Wetting and Spreading," Rev. Mod. Phys., **81**, pp. 739–805.
[28] Shikhmurzaev, Y. D., 2008, *Capillary Flows with Forming Interfaces*, 1st ed, Chapman & Hall/CRC Press, Boca Raton, FL.
[29] Ren, W., Hu, D., and Weinan, E., 2010, "Continuum Models for the Contact Line Problem," Phys. Fluids, **22**, p. 102103.
[30] Lamb, H., 1975, *Hydrodynamics*, 6th ed., Cambridge University Press, Cambridge.
[31] Dussan, E. B., 1979, "On the Spreading of Liquids on Solid Surfaces: Static and Dynamic Contact Lines," Annu. Rev. Fluid Mech., **11**, pp. 371–400.
[32] Scardovelli, R., and Zaleski, S., 1999, "Direct Numerical Simulation of Free-Surface and Interfacial Flow," Annu. Rev. Fluid Mech., **31**, pp. 567–603.

[33] Tezduyar, T. E., 2006, "Interface-Tracking and Interface-Capturing Techniques for Finite Element Computation of Moving Boundaries and Interfaces," Comput. Methods Appl. Mech. Eng., **195**, pp. 2983–3000.
[34] Hirt, C. W., and Nichols, B. D., 1981, "Volume of Fluid (VOF) Method for the Dynamics of Free Boundaries," J. Comput. Phys., **39**, pp. 201–225.
[35] Gueyffier, D., Li, J., Nadim, A., Scardovelli, R., and Zaleski, S., 1999, "Volume-of-Fluid Interface Tracking with Smoothed Surface Stress Methods for Three-Dimensional Flows," J. Comput. Phys., **152**, pp. 423–456.
[36] Sussman, M., Smereka, P., and Osher, S., 1994, "A Level Set Approach for Computing Solutions to Incompressible Two-Phase Flow," J. Comput. Phys., **114**, pp. 146–159.
[37] Sethian, J. A., 2003, "Level Set Methods for Fluid Interfaces," Annu. Rev. Fluid Mech., **35**, pp. 341–372.
[38] Caginalp, G., 1986, "An Analysis of a Phase Field Model of a Free Boundary," Arch. Ration. Mech. Anal., **92**, pp. 205–245.
[39] Anderson, D. M., McFadden, G. B., and Wheeler, A. A., 1998, "Diffuse-Interface Methods in Fluid Mechanics," Annu. Rev. Fluid Mech., **30**, pp. 139–165.
[40] Donea, J., Fasoli-Stella, P., and Giuliani, S., 1976, "Finite Element Solution of Transient Fluid- Structure Problems in Lagrangian Coordinates," Proceedings of the International Meeting on Fast Reactor Safety and Related Physics, Chicago, Illinois, 5–8 Oct., Vol. 3, pp. 1427–1435.
[41] Fukai, J., Zhao, Z., Poulikakos, D., Megaridis, C. M., and Miyatake, O., 1993, "Modeling of the Deformation of a Liquid Droplet Impinging upon a Flat Surface," Phys. Fluids A, **5**, pp. 2588–2599.
[42] Hughes, T. J. R., Liu, W. K., and Zimmermann, T. K., 1981, "Lagrangian-Eulerian Finite Element Formulation for Incompressible Viscous Flows," Comput. Methods Appl. Mech. Eng., **29**, pp. 329–349.
[43] Donea, J., Giuliani, S., and Halleux, J. P., 1982, "An Arbitrary Lagrangian-Eulerian Finite Element Method for Transient Dynamic Fluid-Structure Interactions," Comput. Methods Appl. Mech. Eng., **33**, pp. 689–723.
[44] Christodoulou, K. N., and Scriven, L. E., 1992, "Discretization of Free Surface Flows and other Moving Boundary Problems," J. Comput. Phys.,**99**, pp. 39–55.
[45] Hirt, C. W., Amsden, A. A., and Cook, J. L., 1997, "An Arbitrary Lagrangian-Eulerian Computing Method for all Flow Speeds," J. Comput. Phys.,**135**, pp. 203–216.
[46] COMSOL AB, 2008, COMSOL Multiphysics Modeling Guide, Version 3.5, COMSOL, Columbus, OH.
[47] Winslow, A. M., 1966, "Numerical Solution of the Quasilinear Poisson Equation in a Nonuniform Triangle Mesh," J. Comput. Phys., **1**, pp. 149–172.
[48] Knupp, P. M., 1999, "Winslow Smoothing on Two-Dimensional Unstructured Meshes," Eng. Comput., **15**, pp. 263–268.
[49] Zienkiewicz, O. C., Taylor, R. L., and Zhu, J. Z., 2005, *The Finite Element Method: Volume 1 - Its Basis and Fundamentals*, 6th ed., Butterworth-Heinemann, Amsterdam/Boston.
[50] Christodoulou, K. N., and Scriven, L. E., 1988, "Finding Leading Modes of a Viscous Free Surface Flow: An Asymmetric Generalized Eigenproblem," J. Sci. Comput., **3**, pp. 355–406.
[51] Sisko, A. W., 1958, "The Flow of Lubricating Greases," Ind. Eng. Chem., **50**, pp. 1789–1792 (1958).